

Numerical simulations of the flow of dilute polymer solutions in a four-roll mill

J. Feng, L.G. Leal

Department of Chemical Engineering, University of California, Santa Barbara, CA 93106, USA

Received 12 November 1996; accepted 27 March 1997

Abstract

We study the startup flow of dilute polymer solutions in a four-roll mill by using FENE dumbbell models. Because this flow is inhomogeneous and contains an extension-dominated region at the stagnation point, strong coupling between the flow field and the polymer configuration can be expected. Our effort at simulating such flows and making meaningful comparisons with experiments is a major step toward assessing and improving molecularly-based constitutive models for dilute solutions. The first objective of the paper is to examine the behavior of the Chilcott–Rallison version of the FENE model (FENE-CR) with varying parameters c , De and L . At moderately high values of De and L , the polymer stretching mainly happens within a ‘birefringent strand’ along the exiting flow axis emanating from the stagnation point. The coupling between flow and polymer stretching is exhibited by concerted flow suppression and reduction of polymer extension. In particular, the model predicts double-humped velocity and strain rate profiles across the outflow axis, in qualitative agreement with experiments. The second objective of the paper is to examine the effects of two additional features that can be added to the basic FENE-CR model: shear-thinning and an extra viscous stress. For shear-thinning we use the FENE-P model and for the viscous stress we adopt the expression recently proposed by Rallison [J. Non-Newtonian Fluid Mech., 68 (1977) 61–83]. For the Deborah numbers studied here, shear-thinning causes a small increase in the steady-state polymer stretching at the stagnation point. The strain rate there is also somewhat higher than the corresponding FENE-CR value. The extra viscous stress tends to reduce polymer stretching and the strain rate at the stagnation point. In previous studies, the FENE-CR model has been shown to over-predict polymer stretching. Thus, the extra viscous stress will bring predictions of the model closer to experiments. © 1997 Elsevier Science B.V.

Keywords: FENE model; Four-roll mill; Polymer

1. Introduction

The capability of predicting complex polymer flows in processing has two essential components: a constitutive model that adequately characterizes the material and a numerical algorithm that is able to solve the constitutive equation coupled with flow equations. Recently, great

progress has been made on achieving convergent and accurate solutions at high Deborah numbers, and the constitutive model has become by far the more pressing issue of the two [1]. Interestingly, development of efficient numerical methods opens a new channel for assessing constitutive models, i.e. computing non-homogeneous flows with selected models and comparing the results with experimental measurements made in similar flows. Non-homogeneity is a key word in this context. The first thing one would do to test a constitutive equation is to compare its predictions in simple shear and elongational flows with rheometric measurements. This is fundamentally important but has proven inadequate. The reason is two-fold. First, it is difficult, if not impossible, to generate flows of homogeneous rate of deformation in the laboratory. This is particularly true for purely extensional flows; a large literature has developed on the art of producing such flows and making accurate measurements (e.g. see [2,3]). Thus, one needs knowledge of non-homogeneous flows in order to interpret data obtained in real flows that are approximately homogeneous in a localized region. Second, behavior of complex fluids in non-homogeneous flows often cannot be anticipated from their behavior in homogeneous flows [4], and non-homogeneous flows are invariably what one finds in polymer processing.

To evaluate constitutive equations by carrying out numerical and experimental studies in parallel, we have to decide what flows and constitutive models to study. The flow will have at least localized regions in which the flow field is strongly coupled with the configuration of the polymer. Two-dimensional flows are preferred to three-dimensional ones because flow birefringence, the most frequently measured indicator for polymer orientation and stretch, gives only cumulative effects along the light path and thus is difficult to interpret for three-dimensional structures. In our laboratory, we have used the two-roll mill and the four-roll mill to generate two-dimensional flows [5]. By controlling the relative rotation rates of the rollers (for the four-roll mill) or the ratio of roller radius to gap width between rollers (for the two-roll mill), one may produce a spectrum of locally linear flows between simple shear and pure extension. An attractive feature of these devices is the central stagnation point which affords large strain for stretching polymers. Recently, numerical simulations have been carried out for the two-roll mill [6] and compared with birefringence data [7]. For comparison between numerical simulations and experimental measurements, the four-roll mill offers some advantages over the two-roll mill. Firstly, a wider range of flows can be generated in the four-roll mill. In particular, the two-roll mill cannot access flows close to pure extension even for a Newtonian fluid, and the flow becomes even weaker when modified by polymer stress [6]. Secondly, when operating in the mode of pure extension, the four-roll mill has a fixed outflow axis, and this greatly facilitates study of the relaxation process downstream of the stagnation point. Finally, the symmetry of this extensional flow in the four-roll mill means that the only flow modification by the polymer in the region around the stagnation point is in the magnitude of the velocity gradient. In this sense, flow in the four-roll mill is simpler than that in the two-roll mill and more suitable for the comparative studies we are to undertake. In this paper, we will concern ourselves only with the 'normal mode' of purely extensional flows in the four-roll mill.

Constitutive equations derived from kinetic theory of polymer molecules suit our purpose better than phenomenological models. The former explicitly show the coupling between polymer configuration and fluid flow, and the results are directly comparable with polymer configurations measured through flow birefringence. We have been using the FENE dumbbell models in simulating the flow of dilute polymer solutions. The Chilcott–Rallison version of the model

(FENE-CR) and the effects of conformation–dependent friction have been examined in the two-roll mill [6,8]. The emphasis of the present work will be on the FENE-CR model. In addition, we will report preliminary studies of the shear-thinning FENE-P model and the FENE model with an extra viscous stress recently proposed by Rallison [9]. A parametric study of the FENE-CR model is designed to reveal the sensitivity of its behavior to the model parameters. On the other hand, comparison with models with added features will illuminate the effects of the physical assumptions inherent in the models and suggest whether they approximately represent the true behavior of the polymer molecules.

On the experimental side, systematic studies of the conformation change of polymers in extension-dominated flows were pioneered by a group at the University of Bristol. Extensional flows were generated by using opposed jets [10], the two-roll mill [11], the four-roll mill [12] and cross-slots [13]. Two French groups did similar work in the two-roll mill [14,15] and cross-slots [16,17]. Birefringence patterns were recorded for dilute, semi-dilute and concentrated solutions and velocity profiles are measured by LDV. Experiments in our group have concentrated on the two-roll and four-roll mills. A two-color flow birefringence measurement system has been used to study the stretch and alignment of polymer chains. Dynamic light scattering is used to take simultaneous measurements of the velocity gradient in the flow. Dilute solutions have been studied by Fuller and Leal [18], Dunlap and Leal [19] and Dunlap et al. [20] and semi-dilute and concentrated solutions by Ng and Leal [21], Fuller and Leal [22], Geffroy and Leal [23,24] and Yavich, Mead and Leal [25]. Previous experiments on dilute solutions in our laboratory have focused on steady flows. Recently we have started a systematic study of dilute solutions in transient flows in the two-roll and four-roll mill [7], which will parallel the current series of numerical simulations using the FENE dumbbell models.

The work of the UK and French groups has been summarized by Keller and Odell [26] and Keller et al. [27]. The main findings are as follows. A critical concentration c^+ is identified, which is one order of magnitude smaller than c^* , the concentration of domain overlap for polymers in the coiled state. For $c < c^+$, no flow modification can be discerned even for the largest flow-rate (or Deborah number De). Flow birefringence is restricted to a very thin strand along the outgoing streamline emanating from the stagnation point. The width of the birefringent strand increases with increasing c and De but has an upper bound. For $c > c^+$, the birefringent strand broadens with increasing De until a dark line of non-birefringent (or weakly birefringent) fluid emerges in the middle of the birefringent strand, giving rise to the so-called birefringent pipe. This is also when flow modification is first detected; in a cross-slot device, the velocity profile across the slow downstream of the stagnation point develops a dip at the apex. At still higher De , instability sets in and the flow becomes unsteady.

The above picture raises the question of flow modification in dilute solutions ($c < c^+$). If the birefringent pipe, which occurs only in semi-dilute and concentrated solutions, is a result of the strain rate being suppressed in the middle [27], this signals a very severe degree of flow modification. It is then natural to expect milder and evolving flow modifications before the birefringent pipe emerges and also in more dilute solutions. With direct measurements the velocity gradient, Dunlap and Leal [19] were able to resolve the relatively small flow modifications in dilute solutions. There is no flow modification if the Deborah number is below the critical value for the coil-stretch transition; the onset of flow modification seems to correlate with a certain degree of polymer stretching. The suppression of the local velocity gradient

becomes more severe with increasing De and c . Based on these results, a more consistent picture emerges about the coupling of fluid flow and polymer configuration in dilute solutions. Since the FENE dumbbell models studied here do not account for interactions among stretched polymer chains, experiments in dilute solutions form the basis for comparison with our numerical results.

The outline of the paper is as follows. The numerical problem will be described in Section 2. Numerical results will be reported in Section 3 for the FENE-CR model and in Section 4 for FENE models with additional features. Finally, the main conclusions of the paper will be summarized in Section 5.

2. Formulation of the problem

The geometry of the four-roll mill flow cell is shown in Fig. 1. The four rollers are initially at rest and abruptly start to rotate with angular velocity Ω at time $t = 0$. The fluid is a dilute polymer solution in a Newtonian solvent. With the fluid inertia neglected, the flow equations are

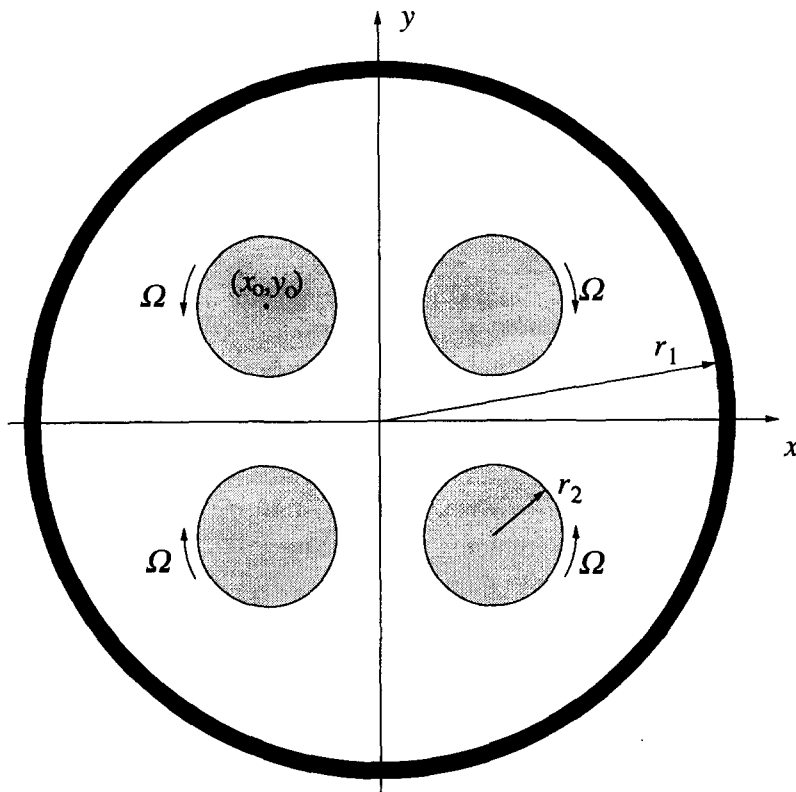


Fig. 1. A sketch of the four-roll mill flow cell. $r_2/r_1 = 0.204$, $(x_0, y_0) = (-0.33, 0.33)r_1$.

$$\begin{cases} \nabla \cdot \mathbf{u} = 0, \\ \rho \frac{\partial \mathbf{u}}{\partial t} = -\nabla p + \mu_s \nabla^2 \mathbf{u} + \nabla \cdot \boldsymbol{\tau}, \end{cases} \quad (1)$$

where $\boldsymbol{\tau}$ is the extra stress due to the polymer, ρ is the density of the solution and μ_s is the solvent viscosity. If one models a polymer chain by a dumbbell, its configuration is simply represented by an end-to-end vector \mathbf{R} . Then the polymer stress is proportional to a configuration tensor which is the second moment of the configuration distribution function [28]: $\mathbf{A} = \langle \mathbf{R}\mathbf{R} \rangle$. The trace of the second moment tensor $\text{tr } \mathbf{A} = \langle R^2 \rangle$ is a measure of the average length of the polymer chain.

In the Chilcott–Rallison model, the finitely extensible elastic spring has a maximum length L and the spring force obeys the Warner force law. After using the pre-averaged spring length in the spring force along with other approximations, the following constitutive model is obtained [29]:

$$\boldsymbol{\tau} = \frac{\mu_s c f(\text{tr } \mathbf{A})}{\lambda} \mathbf{A}, \quad (2)$$

$$\frac{\partial \mathbf{A}}{\partial t} + \mathbf{u} \cdot \nabla \mathbf{A} - (\nabla \mathbf{u})^T \cdot \mathbf{A} - \mathbf{A} \cdot \nabla \mathbf{u} = \frac{f(\text{tr } \mathbf{A})}{\lambda} (\mathbf{I} - \mathbf{A}), \quad (3)$$

where \mathbf{I} is the unit tensor, λ is the relaxation time of the spring and

$$f(\text{tr } \mathbf{A}) = \frac{1}{1 - \text{tr } \mathbf{A}/L^2}.$$

c is the concentration parameter defined by $c = (\mu - \mu_s)/\mu_s$ where μ is the shear viscosity of the solution. For shear-thinning versions of the FENE model (e.g. FENE-P), μ is taken to be the zero shear-rate viscosity of the solution. In Eqs. (2) and (3), \mathbf{A} has been scaled such that $\mathbf{A} = \mathbf{I}$ when there is no flow; L is scaled using the same length.

For a Stokes flow in the four-roll mill, the angular velocity of the roller Ω is linearly related to the velocity gradient (or elongation rate) at the stagnation point $\dot{\gamma}_0$. If we use r_1 as the characteristic length, $r_1 \dot{\gamma}_0$ as the characteristic velocity and $\dot{\gamma}_0^{-1}$ as the characteristic time, the governing equations can be made dimensionless:

$$\nabla \cdot \mathbf{u} = 0, \quad (4)$$

$$\text{Re} \frac{\partial \mathbf{u}}{\partial t} = -\nabla p + \nabla^2 \mathbf{u} + \frac{c}{\text{De}} \nabla \cdot (f\mathbf{A}), \quad (5)$$

$$\frac{\partial \mathbf{A}}{\partial t} + \mathbf{u} \cdot \nabla \mathbf{A} - (\nabla \mathbf{u})^T \cdot \mathbf{A} - \mathbf{A} \cdot \nabla \mathbf{u} = \frac{f(\text{tr } \mathbf{A})}{\text{De}} (\mathbf{I} - \mathbf{A}), \quad (6)$$

where p has been scaled by $\mu_s \dot{\gamma}_0$. The Reynolds number $\text{Re} = \rho r_1^2 \dot{\gamma}_0 / \mu_s$ and the Deborah number $\text{De} = \lambda \dot{\gamma}_0$. The problem thus contains seven dimensionless parameters: Re , De , c , L , r_2/r_1 , x_0/r_1 and y_0/r_1 . Eq. (6) describes how the flow field stretches and orients the polymer and Eq. (5)

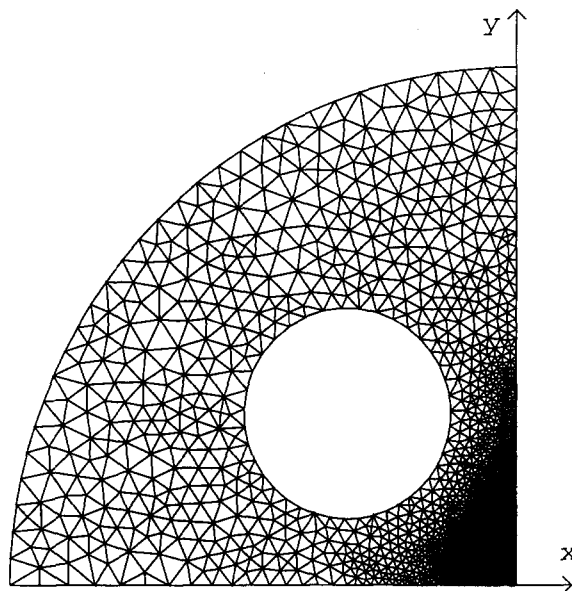


Fig. 2. A typical mesh used in the computations. Only pressure elements are shown. The mesh has 5596 elements and 11 490 nodes, and the number of unknowns is 60 397.

shows how the polymer configuration modifies the flow field in return. In other words, these equations describe the coupling between the configuration of microstructures (\mathbf{A}) and the macroscopic flow field (\mathbf{u} and p). Dirichlet boundary conditions are specified for \mathbf{u} and no boundary condition is needed for \mathbf{A} because of the hyperbolic nature of Eq. (6).

Eqs. (4)–(6) are solved by using a finite element method; the algorithm has been described by Singh and Leal [30]. Here we only note two key features of the code: a third-order upwinding scheme for the convection term ($\mathbf{u} \cdot \nabla \mathbf{A}$) in Eq. (6) and a special procedure to ensure the positive-definiteness of the configuration tensor \mathbf{A} . These features help make the code accurate, efficient and capable of computing flows at relatively high Deborah numbers. Because of the symmetry of the flow cell, we need only use a quarter of the domain in calculation; a typical mesh is shown in Fig. 2. Because of the strong stretching of polymers in the extensional flow, large stress gradients arise which require sufficiently refined mesh to resolve. This proves to be cumbersome because progressively finer mesh is needed for larger values of De or L . For a set of parameters, several meshes often have to be tested and convergence confirmed. Because the four-roll mill generates a stronger flow than the two-roll mill, this requirement on mesh refinement is more stringent than in [6].

The geometry of the flow cell was set so that it matches the flow device used in our experiments: $r_2/r_1 = 0.204$, $(x_0, y_0) = (-0.33, 0.33)r_1$. In the next section, we fix the Reynolds number $Re = 0.136$ and systematically investigate the effects of c , De and L for the FENE-CR model. In Section 4, other forms of the FENE dumbbell model will be discussed along with numerical results.

3. Numerical results for the FENE-CR model

Numerical simulations have been carried out for $De = 0.335\text{--}4.02$, $c = 0, 0.1$ and 1 and $L^2 = 100\text{--}1000$. As c represents the fractional viscosity contribution from the polymer, it is proportional to the polymer concentration in a dilute solution; the coefficient of proportionality depends on the polymer's molecular weight and solvent quality among other factors. From the intrinsic viscosity data of Dunlap and Leal [19], $c = 0.1$ corresponds to roughly 200 ppm of a polystyrene sample of $M_w = 8.42 \times 10^6$ in a Chlorowax LV solvent. In an ideal solvent, the contour length of a polymer chain is proportional to the square-root of the number of Kuhn steps. Based on a molecular weight $M_w \sim 10^6$, the dimensionless parameter L in our dumbbell model may be roughly estimated to be $20 < L < 50$. As mentioned above, large L entails a refined mesh and high cost of computation. In our geometry, the behavior of the dumbbell model does not vary qualitatively with L and we have done the majority of the calculations with $L = 20$.

3.1. The limit of infinite diluteness: $c = 0$

$c = 0$ represents the limiting case where the polymer does not produce any change in the flow but is allowed to deform under the Stokes flow. The significance of this idealized situation lies in the fact that the conformational evolution of the polymer can be examined without the complication of flow modification. So this serves as a probe on polymer stretching on the one hand and as a baseline for studying coupled flow modification and polymer deformation on the other.

3.1.1. Evolution of polymer configuration after startup

The flow field approaches its steady-state very rapidly after the startup; the initial transient takes a dimensionless time $t = 0.033$. Then the configuration of the polymer starts to evolve under the steady Stokes flow. The kinematic features of this flow are shown in Fig. 3. There is an area around the stagnation point in which the strain rate is uniform and the flow type is nearly purely extensional ($\alpha \approx 1$). We define the strain rate as $\dot{\gamma} = (\mathbf{D}:\mathbf{D}/2)^{1/2}$ where $\mathbf{D} = [\nabla\mathbf{u} + (\nabla\mathbf{u})^T]/2$ is the rate-of-strain tensor. At the stagnation point and along the x - and y -axes, $\dot{\gamma}$ is equal to the velocity gradient. On the x - and y -axes near the nips of the roller, there are two localized regions with virtually zero strain rate ($\dot{\gamma} \approx 0$). The flow-type parameter reaches its minimum in these two areas: $\alpha \approx -1$, indicating purely rotational flow. The area next to the roller contains shear flow; the maximum strain rate occurs on the surface of the cylinder. For this geometry, the roller speed and the strain rate at the stagnation point are related by $\Omega = 1.5\dot{\gamma}_0$.

Because of the long residence time of polymer molecules in the region surrounding the stagnation point, the polymer there essentially behaves as in a homogeneous extensional flow. This is borne out by the evolution of $\text{tr } \mathbf{A}$ at the stagnation point (Fig. 4). If the steady-state $\text{tr } \mathbf{A}$ is plotted against De , one will see the coil-stretch transition at a critical Deborah number $De_c = 0.5$. Another interesting feature of Fig. 4 is that the time needed to reach steady state is short for Deborah numbers that are much smaller or larger than De_c , but is very long for $De \approx De_c$. This phenomenon has been discussed by Fuller and Leal [31]. At $De \approx De_c$, the spring

force and the hydrodynamic friction are roughly balanced, and the approach to steady state is largely through Brownian diffusion. Since the strain grows exponentially at the stagnation point, large fractional extension (nearly 90% for $De = 4.02$) of the dumbbell is achieved in a few units of dimensionless time.

The highly homogeneous flow near the stagnation point suggests that the four-roll mill may be used as an extensional rheometer. One may measure the flow birefringence and the velocity

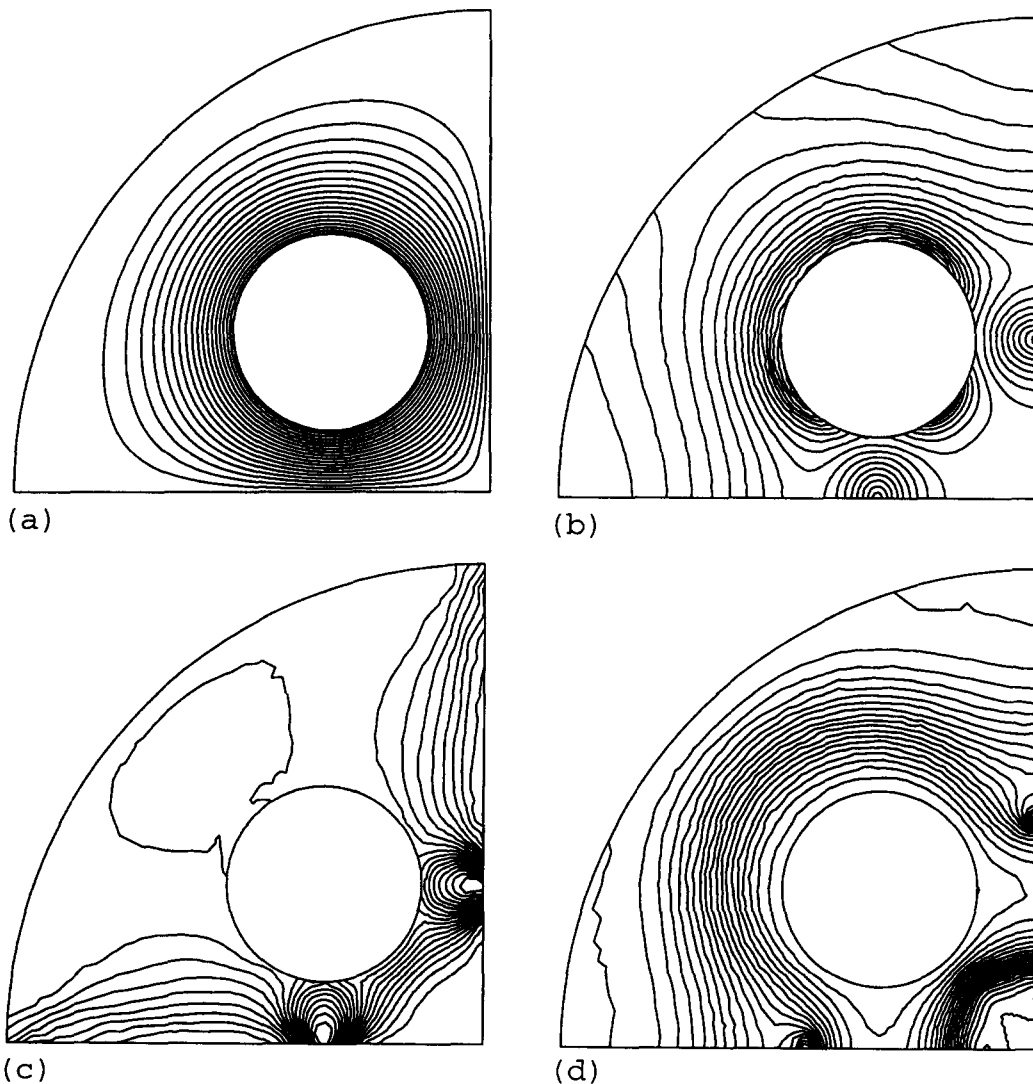


Fig. 3. Kinematic fields of the Stokes flow in the four-roll mill. (a) The streamlines; (b) contours of the strain rate $\dot{\gamma}$. The maximum of $\dot{\gamma}$ occurs on the surface of the roller and the minimum on the two axes where the gap is narrowest between two rollers; (c) contours of the flow type parameters α . The maximum of α occurs at the stagnation point and the minimum on the axes; (d) contours of the residence time. The residence time is longest at the stagnation point and generally decreases toward the roller. See [6] for definitions of the flow type parameter and the residence time.

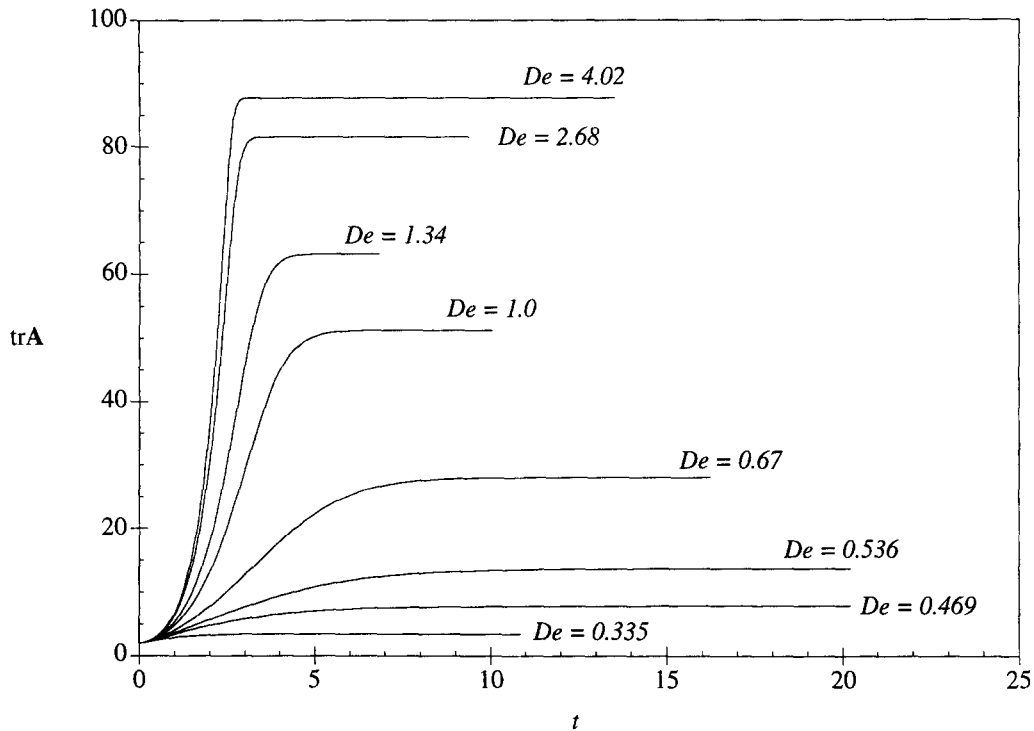


Fig. 4. Stretching of a FENE-CR dumbbell at the stagnation point after startup. The length of the dumbbell is indicated by $\text{tr} \mathbf{A}$. The time is made dimensionless by the steady-state strain rate at the stagnation point $\dot{\gamma}_0$, which is also used in calculating the Deborah number De . $L^2 = 100$.

gradient at the stagnation point and obtain the extensional viscosity through the stress-optic law. This scheme works, of course, only before the stress-optical law is invalidated by nonlinear spring effects.

The evolution of $\text{tr} \mathbf{A}$ in the entire flow cell demonstrates the non-homogeneity of the flow. Fig. 5 shows contours of $\text{tr} \mathbf{A}$ at two different times. At short times ($t = 0.33$ in Fig. 5(a)), the polymer has not sampled a large flow area. The extension of a polymer chain is determined by the flow along the short path that it has travelled. Thus, $\text{tr} \mathbf{A}$ reflects the magnitude of the local strain rate (Fig. 3(b)); the maximum of $\text{tr} \mathbf{A}$ occurs on the surface of the roller. At later times, the maximum of $\text{tr} \mathbf{A}$ moves to the stagnation point, and a thin strip of highly stretched polymer forms along the outgoing flow axis downstream of the stagnation point (Fig. 5(b)). This is evidently the consequence of the long residence time and strong flow near the stagnation point. The fluid far from the x - and y -axes circles around the roller; during each orbit the polymer goes through areas of low strain rate and weak flow type and relaxes. The fluid near the x -axis has a longer residence time, but the deformation history is weak leading to the stagnation point and thus the stretching is weak, too. The highly localized region with stretched polymers downstream of the stagnation point closely resembles the birefringence pattern observed in experiments [12,18], and may be called the ‘birefringent strand’ following Harlen et al. [32].

A more precise view of the evolution of polymer configuration can be gained from the profile of $\text{tr } \mathbf{A}$ along the 45° line between the roller and the stagnation point and along the x - and y -axes (Fig. 6). At short times, the polymer next to the roller starts to stretch first. Later, the maximum of $\text{tr } \mathbf{A}$ shifts to the stagnation point (Fig. 6(a)). The surface of the roller remains a local maximum of $\text{tr } \mathbf{A}$ because of the high shear rate there. The distribution of $\text{tr } \mathbf{A}$ along the two axes is best understood by following the streamlines. At the solid wall ($x = -1$), the strain rate is always zero and the polymer remains relaxed. Off the wall there is a weak converging flow, which gives rise to a mild stretch in the x -direction. As the flow passes through the rotational region (Fig. 3(c)), the polymer relaxes somewhat and then encounters the extensional flow near the stagnation point. The dumbbells are turned to the y -direction and there is a sharp rise in $\text{tr } \mathbf{A}$; the polymer has a long time for stretching within a small neighborhood of the stagnation point. The plateau downstream of the stagnation point represents large stretching sustained by the extensional flow. Further downstream, the polymer passes through the rotational region and again relaxes. There is a weak squeezing flow toward the wall, which leads to mild stretching in the x -direction near $y = 0.7$.

Though the development of $\text{tr } \mathbf{A}$ at the stagnation point is monotonic, it appears to be oscillatory in other regions of the flow cell (Fig. 6(a)). This is more conspicuous at larger De . Fig. 7 shows the history of $\text{tr } \mathbf{A}$ at the point P on the roller that is closest to the y -axis (the point is fixed in space, not attached to the roller). The oscillatory behavior highlights the non-homogeneity of the flow. Since the residence time next to the roller is much shorter than the relaxation time of the polymer, the polymer does not have enough time to relax and thus ‘remembers’ its flow history. So an Eulerian point in space sees the arrival of polymer molecules that carry different deformation histories since the start of the flow. Because of the variation of $\dot{\gamma}$ around the roller (see Fig. 3(b)), strongly and weakly stretched polymers show up alternately at a point

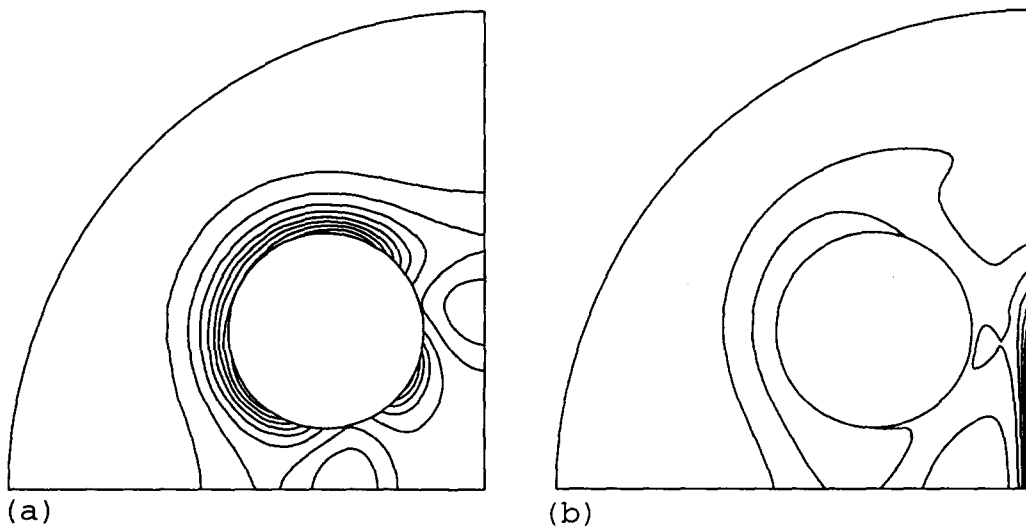


Fig. 5. Contours of $\text{tr } \mathbf{A}$ at an early and a late stage of stretching. $L^2 = 100$, $De = 1.34$. (a) Dimensionless time $t = 0.33$; (b) $t = 10$.

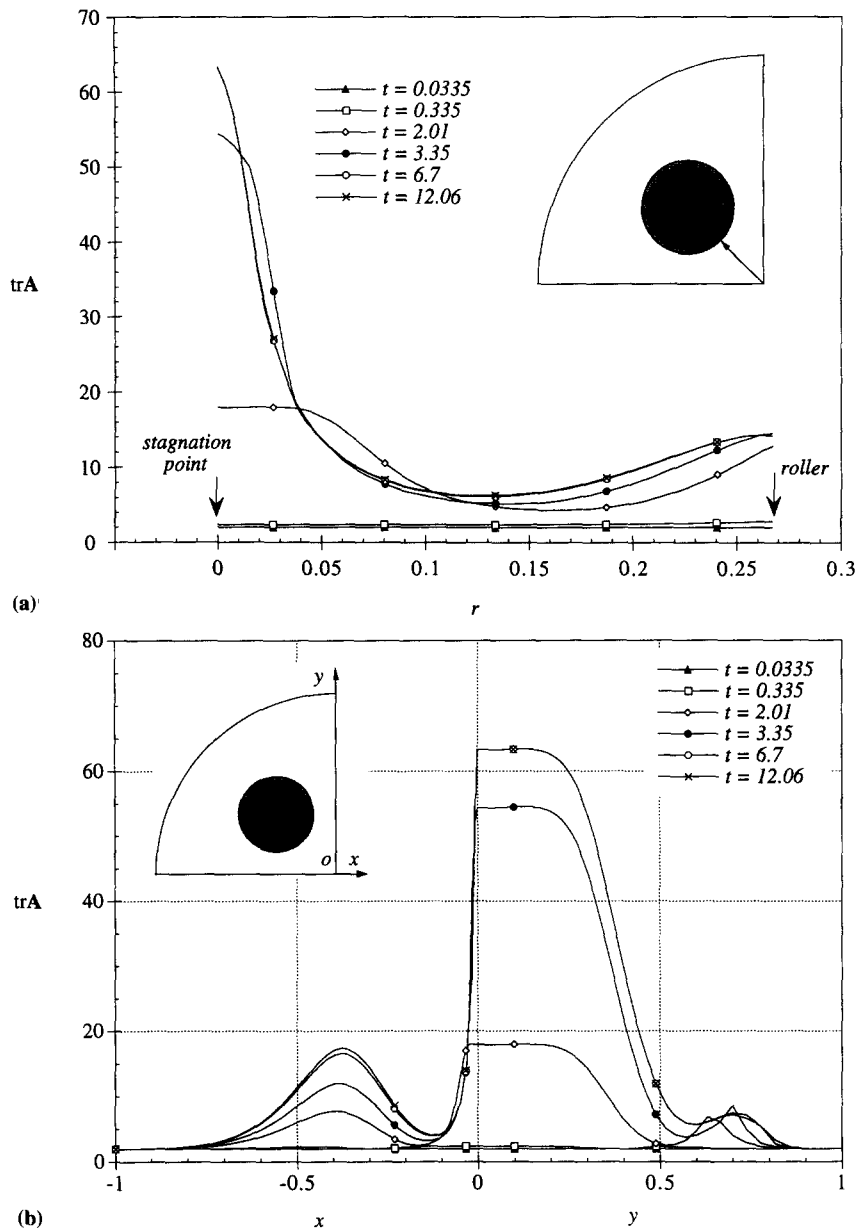


Fig. 6. Evolution of $\text{tr} \mathbf{A}$ profiles after startup. $L^2 = 100$, $De = 1.34$. (a) The profile along the 45° line between the roller and the stagnation point; (b) profiles along the inflow and outflow axes.

fixed in space. After the roller makes a few turns, the history effects start to be smoothed out. During the first turn of the roller, each fluid particle on the roller surface passes the test point P once. After that, each goes through the same cycle of deformation. The temporal variation at P reflects the difference in flow history incurred during the first turn. This difference will fade in time because of the fading memory of the polymer and the addition of more cycles to its

deformation history. Thus, the oscillation at P dies out after a few turns of the roller and a steady state is reached. Incidentally, the FENE dumbbell models yield a monotonic stress growth at the start of a simple shear at moderately low De . For large De , a stress overshoot occurs. This is obviously not the cause of the oscillation in Fig. 7.

The transient in $\text{tr} \mathbf{A}$ due to kinematics of the flow has some interesting implications in experiments. For a dilute solution, the growth of the flow birefringence at the stagnation point is monotonic after startup in a two-roll mill [7]. If the measuring volume is off the stagnation point, however, one may get an oscillatory signal as in Fig. 7, which must not be construed as an intrinsic reaction of the polymer to a uniform extensional flow. For semi-dilute and concentration solutions, the growth of the flow birefringence is not monotonic even in locally homogeneous extensional flows [21]. It is then important to recognize the two possible mechanisms for the transient in a non-homogeneous flow.

3.1.2. Effects of De on the steady state

The effect of De on the steady-state distribution of $\text{tr} \mathbf{A}$ is, in a sense, also not monotonic. At small De , the polymer has a short relaxation time and reacts to the local deformation quickly. Thus the $\text{tr} \mathbf{A}$ contours resemble the $\dot{\gamma}$ contours of the Stokes flow (Fig. 8(a)). At larger De , strong stretching occurs in the birefringent strand along the y -axis and stretching near the roller is relatively weak (Fig. 8(b)). At still larger De , there is a reversal of this trend; the birefringent strand widens and there is again considerable stretching at the roller (Fig. 8(c)). This reversal is manifest of the fact that at $De \gg De_c$, the dumbbell tends to deform more affinely with the fluid and thus needs shorter time to achieve a large fractional stretch. The effect of De in Fig. 8 is

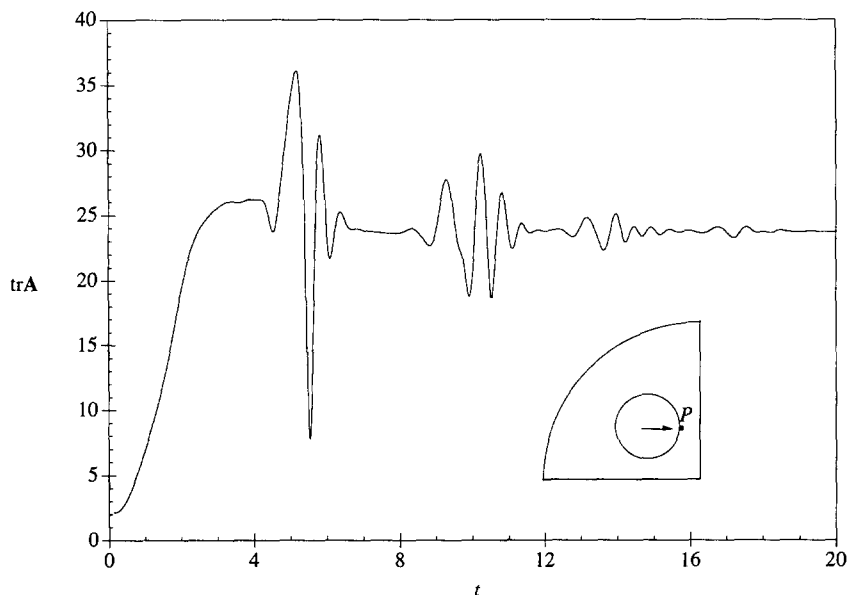


Fig. 7. Transient of $\text{tr} \mathbf{A}$ at a spatial point P that is at the surface of the roller (indicated by an arrow). $L^2 = 100$, $De = 2.68$. The roller makes one turn in time $t = 4.19$ and the residence time at P is only about 7.2% of the relaxation time of the polymer.

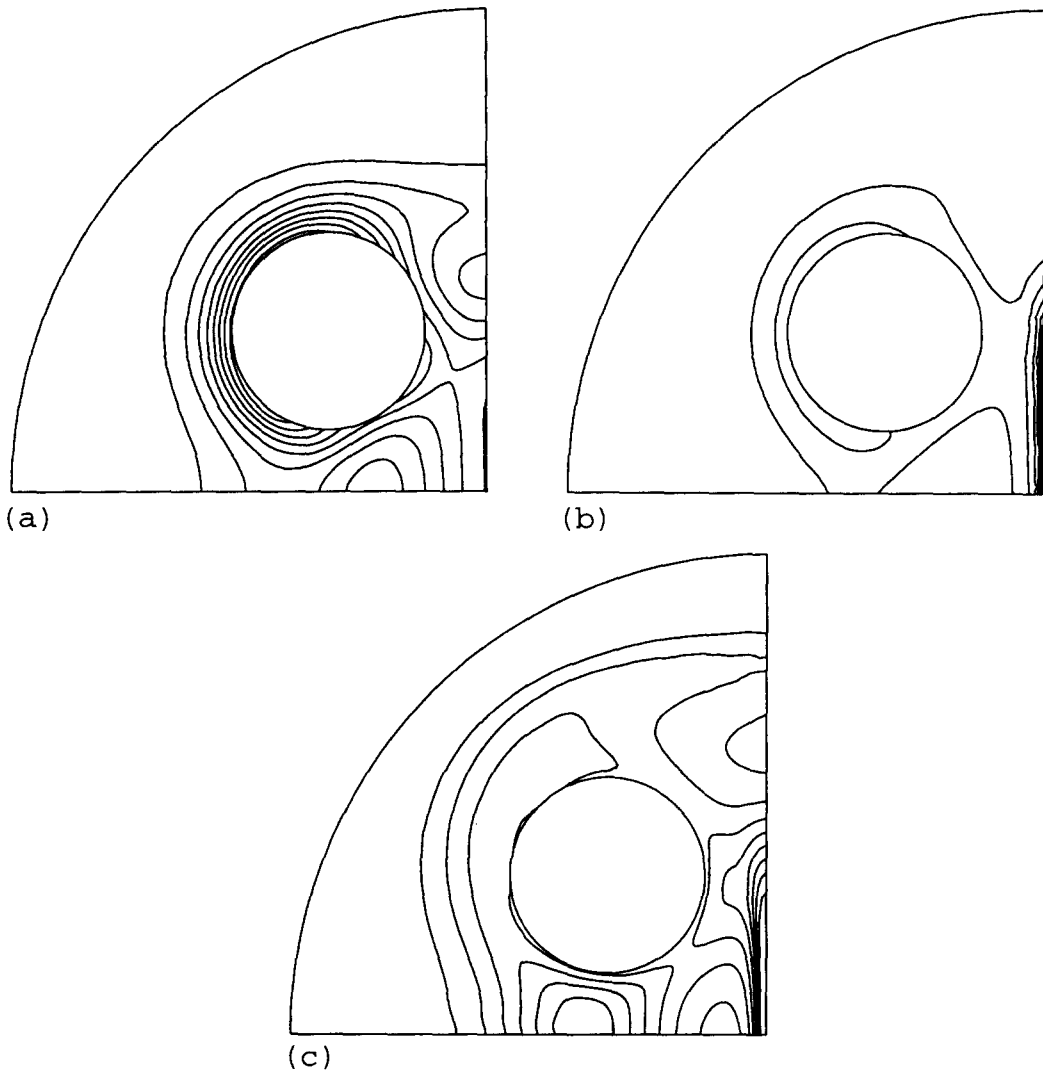


Fig. 8. Comparison of the steady-state $\text{tr } \mathbf{A}$ contours at different Deborah numbers. $L^2 = 100$. (a) $De = 0.335$; (b) $De = 0.67$; (c) $De = 2.68$.

consistent with that in Fig. 4. If the polymer needs a long time to reach steady-state extension, the long residence time at the stagnation point gives rise to a localized birefringent strand. Conversely, if the polymer reaches steady-state extension rapidly (as for very small or large De), the residence time at the stagnation point is less of a factor and the birefringent area is de-localized. The sequence described above is more precisely illustrated by the steady-state $\text{tr } \mathbf{A}$ profiles along the 45° line (Fig. 9). As De increases, there is more stretching everywhere in the flow field. At larger De , the increase in stretching is most prominent near the roller, and a valley forms between the roller and the stagnation point.

3.1.3. Effects of L on the steady state

The effects of L on polymer stretching may be analyzed from two limiting cases. Since L enters Eq. (6) only through the spring force f , it has little effect on the polymer where the stretching is small. The other limit is for very large stretching, in which case the Brownian force is negligible as compared with the spring force. This is tantamount to setting $I - \mathbf{A} \approx -\mathbf{A}$ in Eq. (6), and it becomes obvious that $\text{tr } \mathbf{A}/L^2$ will be independent of L . The two limits are clearly shown by $\text{tr } \mathbf{A}$ profiles along the x - and y -axes (Fig. 10). L has virtually no effect on $\text{tr } \mathbf{A}$ at $x \approx -0.4$ and $y \approx 0.7$, where the stretching is weak and the finite extensibility is hardly felt. On the other hand, the plateau of $\text{tr } \mathbf{A}$ downstream of the stagnation point increases proportionally with L^2 . The temporal evolution of $\text{tr } \mathbf{A}$ at the stagnation point is compared in Fig. 11 for different values of L . The steady-state value of $\text{tr } \mathbf{A}/L^2$ agrees closely among the curves, although it takes longer time to achieve the steady state for larger L . The different behavior of $\text{tr } \mathbf{A}$ in different regions of the flow implies that as L^2 increases, the peak in $\text{tr } \mathbf{A}$ will become more pointed; relatively more stretching happens inside the birefringent strand and less happens in other areas.

Another implication of the above analysis is that the early stage of polymer deformation is independent of L before large fractional stretch happens anywhere. A somewhat more general statement can be made about a startup flow, though based on entirely different arguments: the initial moments of polymer stretching in a dilute solution is independent of all three parameters De , c and L . Before the flow starts, the spring force and the Brownian force are in balance. Thus, the initial stretching will be completely determined by the velocity gradient. Our numerical results show that $\text{tr } \mathbf{A}$ stays independent of L until $t = 0.33$ after the startup. By that time $\text{tr } \mathbf{A}$ already strongly depends on De .

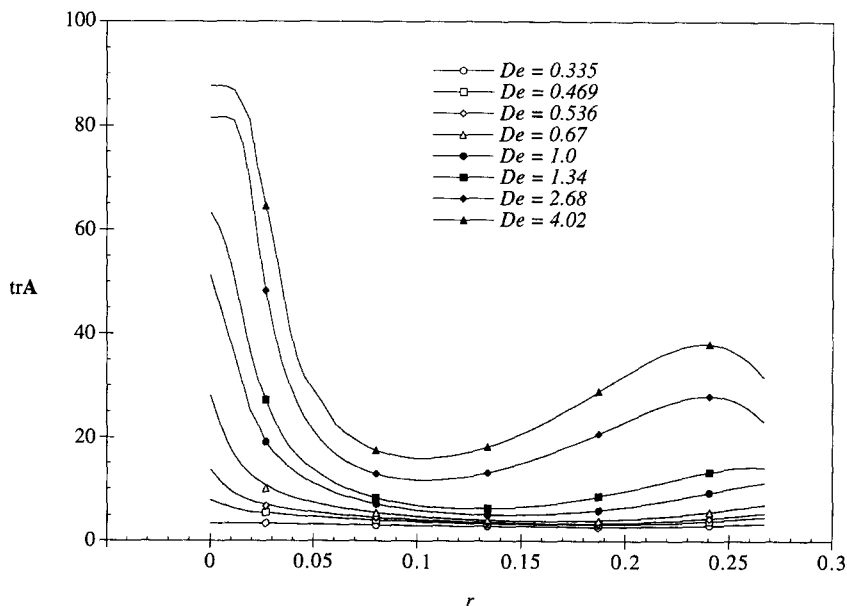


Fig. 9. Comparison of steady-state $\text{tr } \mathbf{A}$ profiles along the 45° line at different Deborah numbers. $L^2 = 100$.

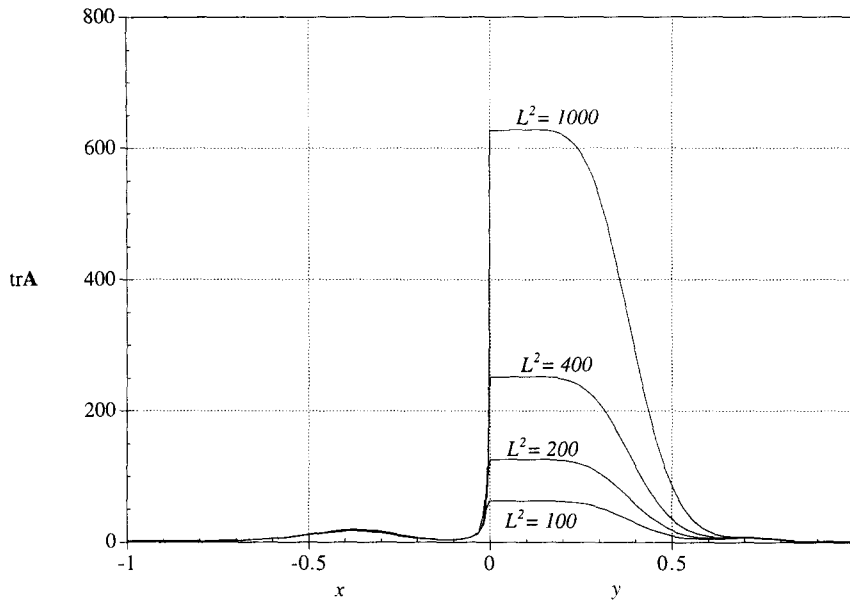


Fig. 10. Comparison of $\text{tr } \mathbf{A}$ profiles along the x - and y -axes for different values of L^2 . $De = 1.34$.

3.2. Coupling of flow and polymer configuration at $c > 0$

In the presence of polymer stress, the strain rate at the stagnation point will be different from $\dot{\gamma}_0$. The calculations reported hereafter are for the same rotation speed Ω of the rollers and the same nominal Reynolds number $Re = \rho r \dot{\gamma}_0 / \mu_s = 0.136$. We will continue to use $\dot{\gamma}_0$ to form the dimensionless time, dimensionless strain rate and the Deborah number.

3.2.1. Flow modification

The effect of polymer stress on the flow is most readily seen from $\dot{\gamma}$ at the stagnation point (Fig. 12(a)). The initial development of the flow field is not affected by the polymer and the fluid quickly assumes the Stokes flow which is the steady state for $c = 0$. Then the polymer starts to stretch, causing $\dot{\gamma}$ at the stagnation point to undershoot before approaching a steady-state value that is smaller than $\dot{\gamma}_0$. The transient of $\dot{\gamma}$ agrees qualitatively with previous results of Harris and Rallison [33], who studied the startup of extensional flows in a cross-slot geometry by asymptotic analysis. Using a dilute polystyrene solution, Harrison et al. [7] measured the velocity gradient at the stagnation point of a two-roll mill after startup. The strain rate $\dot{\gamma}$ rapidly reaches the Newtonian value and then gradually decreases to the steady-state limit; there is no undershoot in this process. Wang et al. [34] did similar measurements on concentrated polystyrene solutions and the evolution of $\dot{\gamma}$ is very similar to the curves in Fig. 12(a); there is an undershoot before $\dot{\gamma}$ approaches its steady-state value. One must note a fundamental difference between the two-roll and four-roll mills. The flow modification at the stagnation point consists in a reduction in $\dot{\gamma}$ in the four-roll mill. In a two-roll mill, the flow type parameter is also seriously reduced by polymer stress [6]. The effect of polymer on the steady-state flow is such

that with increasing c , the flow and deformation of the fluid is enhanced in the area around the roller and suppressed near the stagnation point and the outflow axis where the polymer is highly stretched. Fig. 13 demonstrates this trend in the profile of $\dot{\gamma}$ between the roller and the stagnation point. The flow suppression near the stagnation point and the y -axis is evidently a result of the polymer stress.

The effect of flow suppression agrees qualitatively with the experimental observations of Dunlap and Leal [19] in a four-roll mill. In particular, they measured profiles of the velocity gradient across the outgoing axis at various distances from the stagnation point. Immediately downstream of the stagnation point, the profile develops a dip in the middle, which becomes deeper further downstream. Fig. 14 shows similar profiles from our simulation at a small distance downstream of the stagnation point, along with the profiles of the velocity v and $\text{tr} \mathbf{A}$ at the same station. Curve 1 in Fig. 14(a), for the Stokes flow, has a small decrease in $\dot{\gamma}$ toward the y -axis; this is due to the kinematics of the flow in this geometry. With increasing c , much larger flow suppression happens and this effect also extends farther from the outflow axis. The most interesting feature of Fig. 14(b) is the suppression of the fluid velocity near the y -axis; the profile is very similar to the ‘double-humped’ velocity profiles measured in the cross-slot device [13,16]. The peaks of $\text{tr} \mathbf{A}$ in Fig. 14(c) are extremely narrow, but the influence of the stretched polymer on the fluid flow spreads to a much wider region. This effect has also been observed by Dunlap and Leal [19] in experiments.

3.2.2. Polymer configuration

The change in the flow field in turn leads to changes in the polymer configuration, most conspicuously a reduced stretch at the stagnation point and downstream (Fig. 12(b) and Fig.

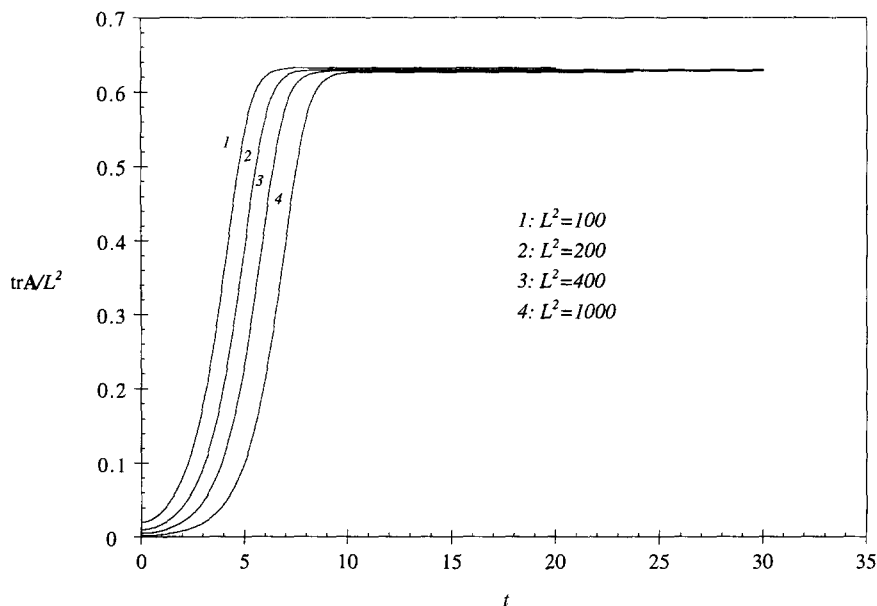


Fig. 11. The evolution of $\text{tr} \mathbf{A}$ at the stagnation point for different values of L^2 . $De = 1.34$.

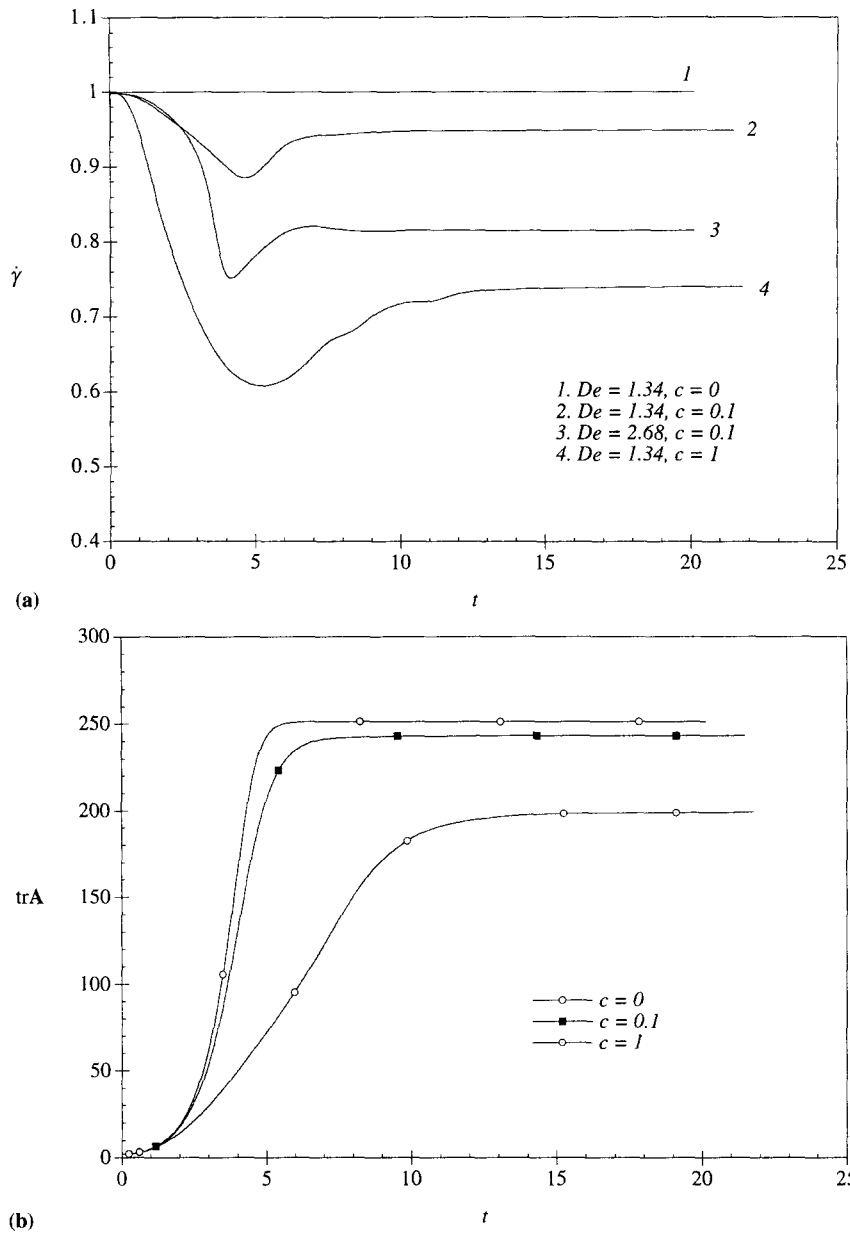


Fig. 12. The evolution of the strain rate $\dot{\gamma}$ (a) and $tr \mathbf{A}$ (b) at the stagnation point for different values of the polymer concentration c . $L^2 = 400$, $De = 1.34$. A curve for a higher Deborah number ($De = 2.68$) is also shown in (a).

14(c)). There is no overshoot in the growth of the birefringence at the stagnation point, consistent with experimental measurements in dilute solutions [7]. Fig. 15 compares the steady-state contours of $tr \mathbf{A}$ at $c = 0.1$ and 1. Apparently with increasing c , the stretching becomes less concentrated in the birefringent strand. This implies a decrease of $tr \mathbf{A}$ near the stagnation point and an increase near the roller, which is consistent with the modification in the

flow discussed above. As a rule, larger c means more severe flow suppression, accompanied by larger decrease in $\text{tr } \mathbf{A}$ at the stagnation point and downstream. Polymer stretching also becomes de-localized.

3.2.3. Coupling of flow and polymer stretching

A more quantitative analysis of the flow-polymer coupling can be done by following the streamline that passes through the stagnation point. Fig. 16 shows steady-state profiles of the velocity, strain rate and the two components of \mathbf{A} along the x - and y -axes. $A_{12} = 0$ because of symmetry.

On the x -axis, Eq. (5) reduces to

$$\frac{\partial^2 u}{\partial x^2} + \frac{\partial^2 u}{\partial y^2} = \frac{dp}{dx} - \frac{c}{\text{De}} \frac{d}{dx} (fA_{11}).$$

Owing to a locally converging flow, A_{11} increases along the x -axis off the wall, the polymer stress gives

$$\frac{d}{dx} (fA_{11}) > 0,$$

which causes a decrease in $\partial^2 u / \partial x^2$, and hence the suppression of u and $\dot{\gamma}$ along the left part of the incoming flow axis ($x < -0.4$). Further down the axis, A_{11} is compressed by the decelerating flow:

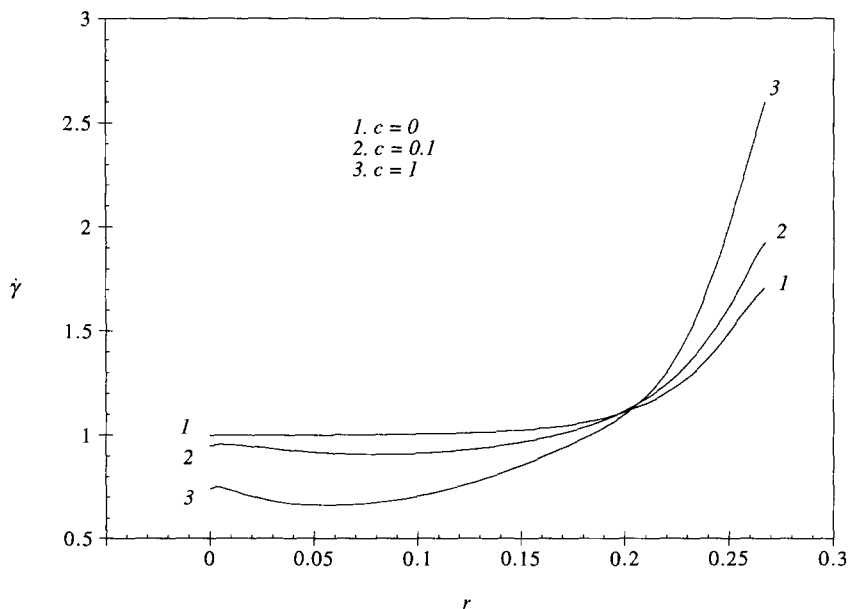


Fig. 13. Effects of polymer concentration on the profile of $\dot{\gamma}$ along the 45° line between the stagnation point ($r = 0$) and the roller ($r = 0.267$). $L^2 = 400$, $\text{De} = 1.34$.

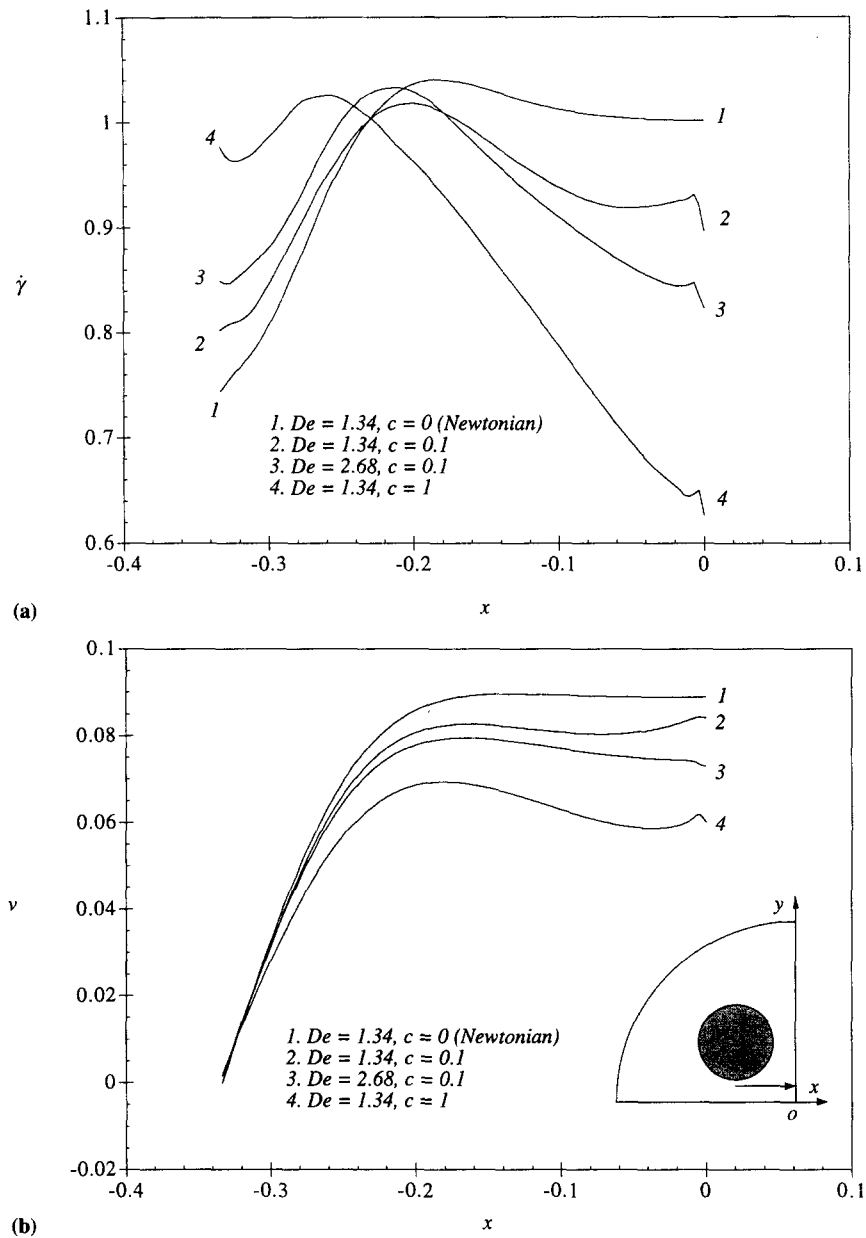


Fig. 14.

$$\frac{d}{dx} (fA_{11}) < 0,$$

and the polymer stress tends to increase $\partial^2 u / \partial x^2$. Since $\partial u / \partial x < 0$, this means a dip in the strain rate $\dot{\gamma}$, as indeed happens in Fig. 16(b). Next to the stagnation point, there is a small but steep increase in A_{11} . This, together with the sharp increase in A_{22} and thus in the spring force, gives a very large stress gradient

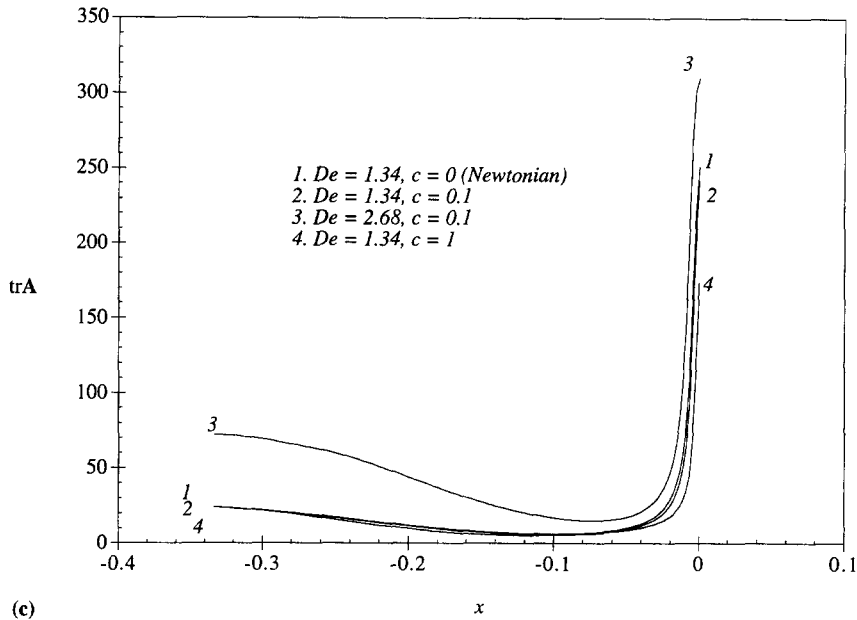


Fig. 14. Effects of polymer concentration on profiles of $\dot{\gamma}$, v and $\text{tr } \mathbf{A}$ downstream of the stagnation point ($y = 0.089$). $L^2 = 400$. The position of the profiles is indicated by a horizontal line in (b). Curve 3, for a higher Deborah number, is also shown for comparison. The small wriggle in the $\dot{\gamma}$ and v profiles next to the y -axis indicates a narrow boundary layer which will be further discussed as related to Fig. 16 and Fig. 19.

$$\frac{d}{dx} (fA_{11}) > 0,$$

which explains the upturn of $\dot{\gamma}$ near $x = 0$. On the y -axis, there is a concerted suppression of flow and polymer stretching.

The above analysis offers some insights on the interplay between the flow and the polymer stress. It may not be appropriate to claim one as the cause of the other, and some of the physics behind the numerical results remains veiled. For example, we see the connection between the sharp rise of A_{11} and the upturn in $\dot{\gamma}$ on the x axis next to the stagnation point. But the reason why such a boundary layer exists is not clear.

3.2.4. Effects of De and L

At larger De the flow suppression becomes more severe. For $L^2 = 400$ and $c = 0.1$, a calculation at $De = 2.68$ is compared with one at $De = 1.34$ in Fig. 12(a) and Fig. 14. The Deborah number, representing strength of the flow, enhances polymer stretching. The larger gradient of polymer stress in turn promotes flow suppression much like the effect of increasing c . Fig. 17 compares the $\text{tr } \mathbf{A}$ profiles for these two runs. As De changes from 1.34 to 2.68, the increase in $\text{tr } \mathbf{A}$ is greater, in percentage, in regions of weak flows ($x \approx -0.3$; $y \approx 0.7$) than at the stagnation point. This is because the nonlinearity of the spring is hardly felt in areas of weak stretching. At the stagnation point, on the other hand, further stretching becomes harder. This is in fact the same mechanism that operates at $c = 0$ to make the stretching more spread out as

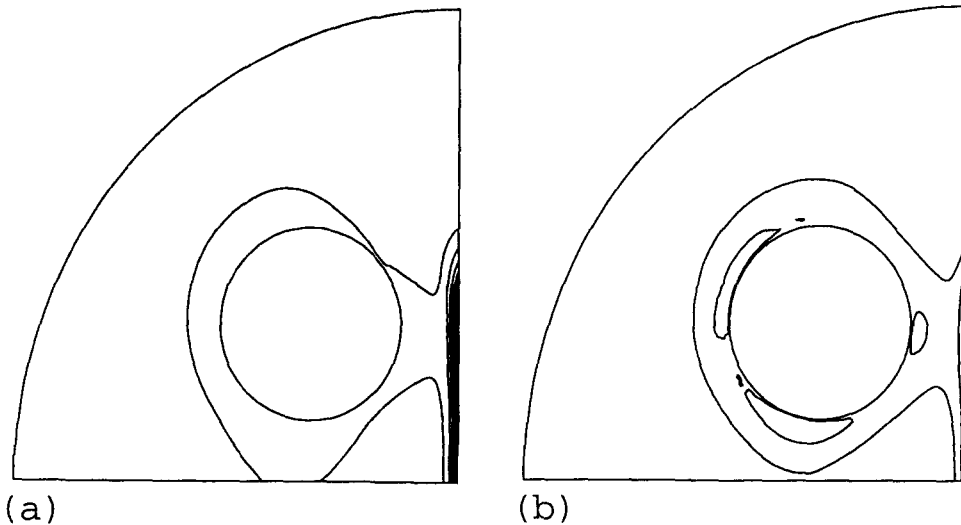


Fig. 15. Steady state contours of $\text{tr } \mathbf{A}$ at different polymer concentration. $L^2 = 400$, $\text{De} = 1.34$. (a) $c = 0.1$; (b) $c = 1$.

De increases (Fig. 8). Similar de-localization of stretching is observed here, but to a lesser degree because of flow modification.

For relatively small c and De , the effects of L on the polymer configuration are qualitatively the same as in the case of $c = 0$. \mathbf{A} increases proportionally with L^2 near the stagnation point and downstream on the y -axis but hardly changes in other regions of the flow (Fig. 18). Therefore, the polymer stress increases linearly with L^2 within the birefringent strand. For larger c and De , the above statements become less accurate because of flow modification. But qualitatively, one may expect that larger L values lead to more severe flow suppression within the birefringent strand, similar in effect to an increase in c (Fig. 14(a) and 14(b)). Profiles of $\dot{\gamma}$ along the x - and y -axes show that at larger L , the flow suppression is indeed more severe except in a ‘boundary layer’ next to the stagnation point (Fig. 19). The climb of $\dot{\gamma}$ toward the stagnation point that has been analyzed in Fig. 16(b) grows with L^2 . For $L^2 = 100$, $\dot{\gamma}$ at the stagnation point even exceeds $\dot{\gamma}_0$, the value for $c = 0$. This implies that for larger L^2 , polymer extension actually enhances the flow in a very localized region. Harrison et al. [7] obtained a similar result using the FENE-CR model in the two-roll mill. To resolve the sharp gradient in the boundary layer, we have used refined mesh in the area (see Fig. 2). There are 38 mesh points within $-0.05 \leq x \leq 0$, which may be considered the width of the boundary layer. Hence the boundary layer is not an artifact due to poor resolution. Since there has been no experimental evidence for such a flow enhancement, this might indicate a defect of the FENE-CR model. We will return to this issue in the next section as related to the extra viscous stress.

4. Numerical results for other FENE models

In this section we study FENE models with shear-thinning (FENE-P) and extra viscous stress (FENE-V). No parametric matrix will be covered; the focus will be on the effects of the physical assumptions in these models on the flow.

4.1. The FENE-P model

The FENE-P model is very similar to the FENE-CR model except that it has shear-thinning. In general, shear-thinning is not a critical property in FENE dumbbell models, firstly because dilute solutions usually are only mildly shear-thinning and secondly because the FENE-dumbbell models are meant to mimic polymer behavior in extensional flows, not shear flows. In the

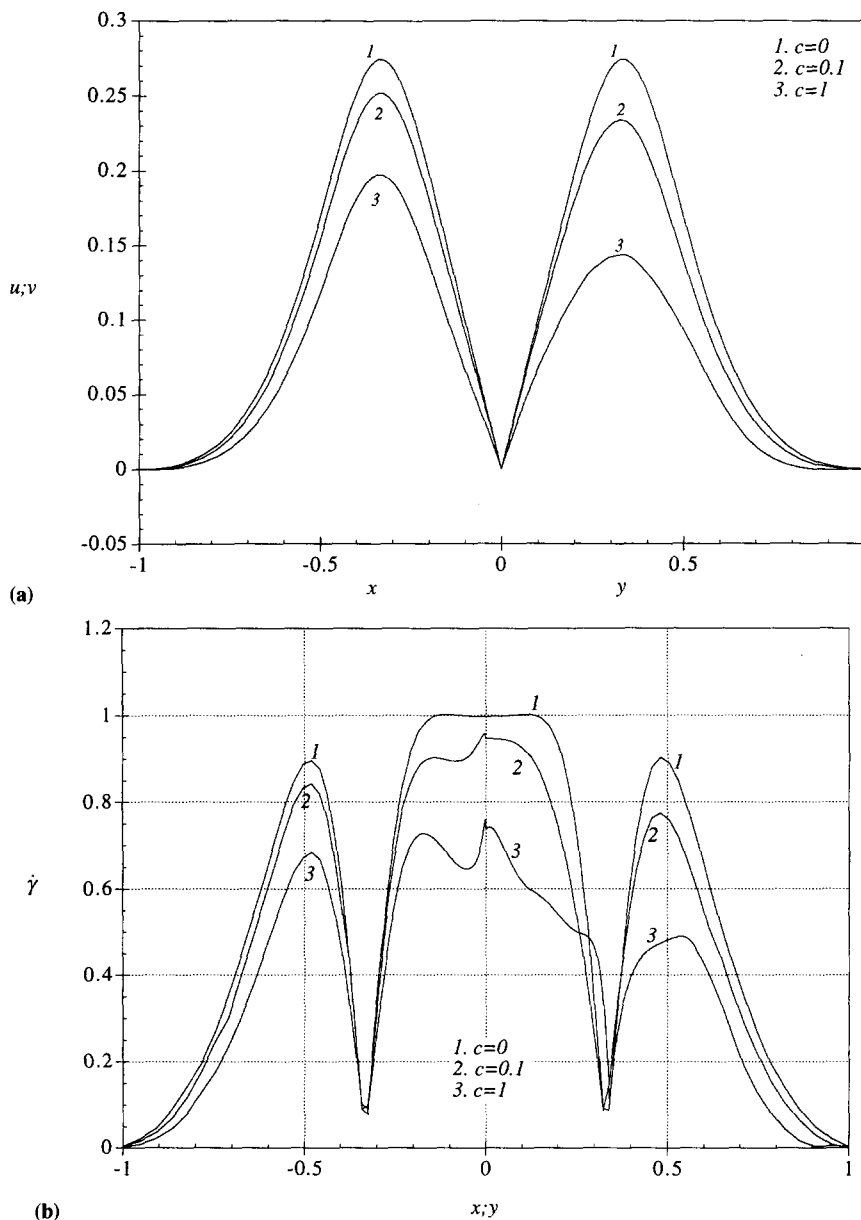


Fig. 16.

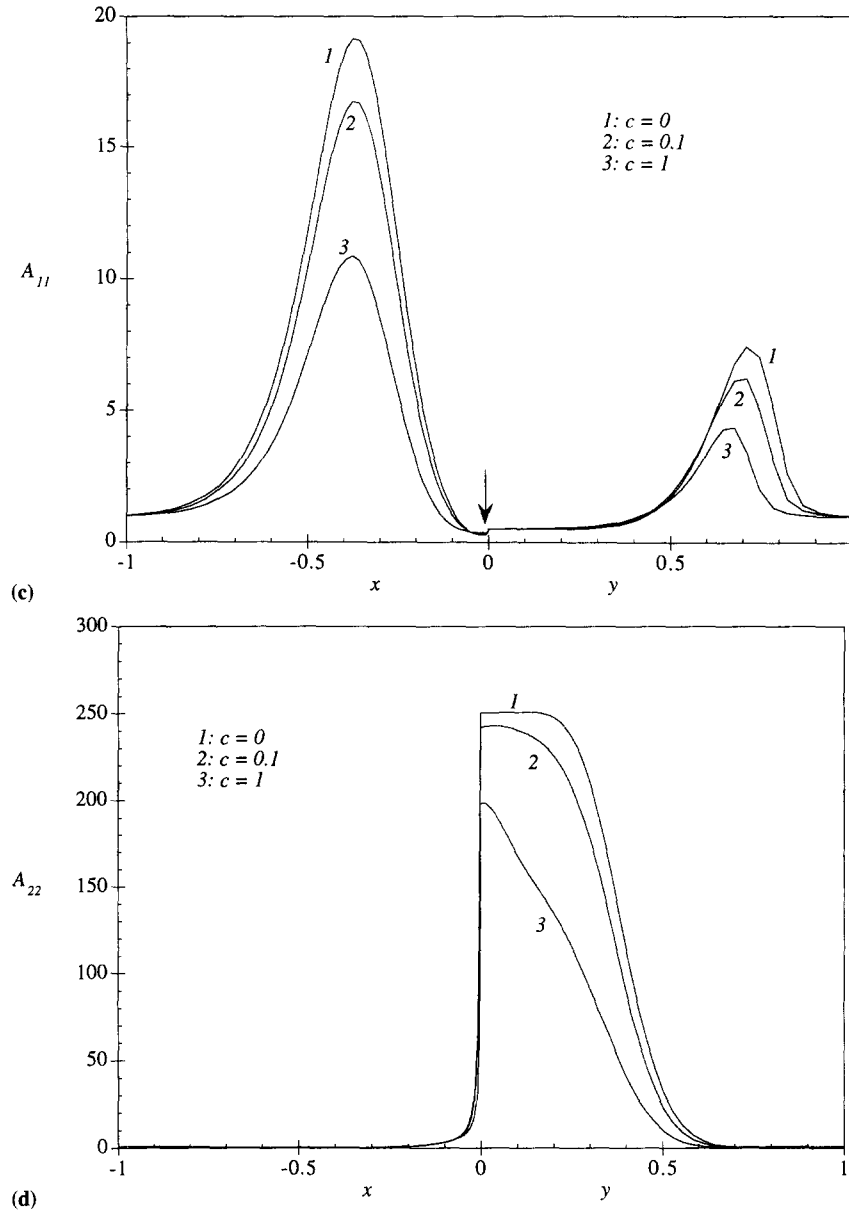


Fig. 16. Coupling between flow and polymer configuration as shown by profiles along the x - and y -axes. $L^2 = 400$, $De = 1.34$. (a) Velocity u along x and v along y ; (b) strain rate $\dot{\gamma}$; (c) A_{11} . The narrow indicates the sharp increase of A_{11} within a ‘boundary layer’ next to the stagnation point; (d) A_{22} .

two-roll and four-roll mills, the flow is driven by the rollers. Changes in the roller speed are transmitted through shear layers toward the stagnation point where measurements are made. Thus the transient at the stagnation point may be affected by shear-thinning and hence our interest in the FENE-P model.

For the FENE-P model, Eq. (6) is changed to

$$\frac{\partial \mathbf{A}}{\partial t} + \mathbf{u} \cdot \nabla \mathbf{A} - (\nabla \mathbf{u})^T \cdot \mathbf{A} - \mathbf{A} \cdot \nabla \mathbf{u} = \frac{1}{De} (\mathbf{I} - f\mathbf{A}).$$

At large De , the shear viscosity varies as $\dot{\gamma}^{-2/3}$ [35,36]. The onset of shear-thinning is at higher De for larger values of L^2 . Therefore, at a given De more shear-thinning occurs for smaller L . Besides L and c , there is no other parameter by which to control the amount of shear-thinning.

Our simulation covers c up to 1, L^2 to 400 and De to 1.34. In all these cases, shear-thinning does not produce a major effect. Fig. 20 shows the evolution of $\dot{\gamma}$ and $\text{tr} \mathbf{A}$ at the stagnation point after a startup in the four-roll mill. There is virtually no shear-thinning effect in the early transient. The steady-state values of $\dot{\gamma}$ and $\text{tr} \mathbf{A}$ are both a little larger than the corresponding values for the CR model. The lack of a strong shear-thinning effect in these calculations is not entirely surprising since for $L^2 = 400$, significant shear-thinning does not set in until De is on the order of 100. Still larger De is needed for $L^2 = O(2000)$, which is more appropriate for the polystyrene solutions we have been using in experiments. Therefore, the FENE-P model, without a separate parameter to adjust the amount of shear-thinning, is not a good choice for testing shear-thinning effects. This, however, may not be a serious shortcoming of the FENE-P as a dilute solution model. The actual magnitude of shear-thinning effects in extension-dominated flows, to our knowledge, has not been documented experimentally.

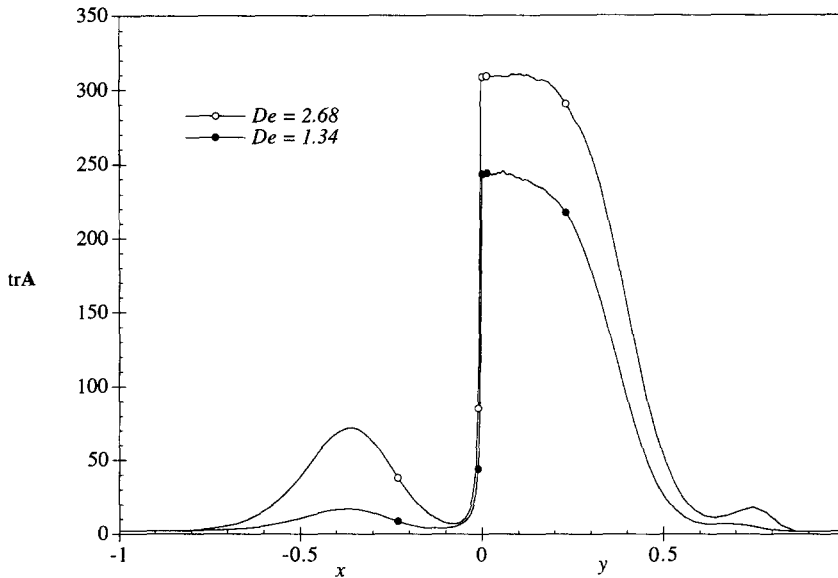


Fig. 17. Effects of De on the profiles of $\text{tr} \mathbf{A}$ along the axes. $L^2 = 400$, $c = 0.1$.

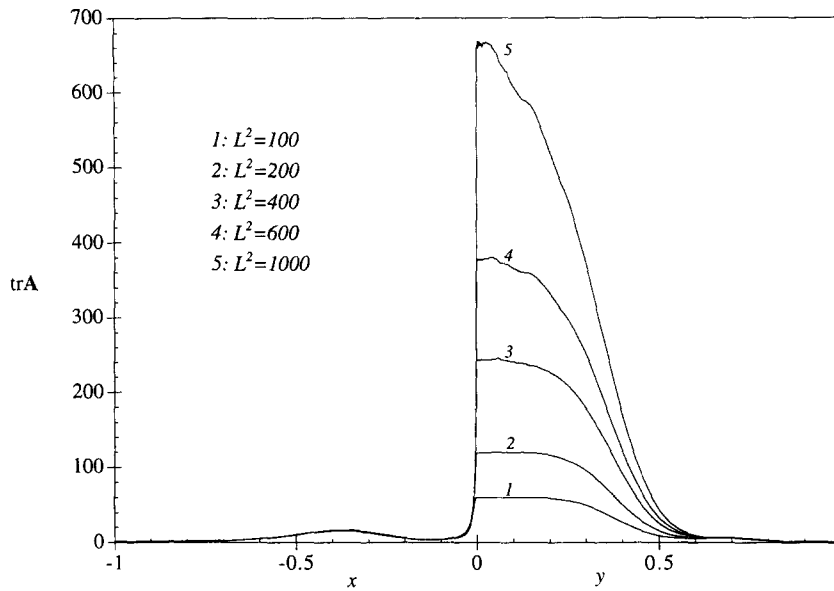


Fig. 18. Effects of L on the $\text{tr } \mathbf{A}$ profiles along the axes. $De = 1.34$, $c = 0.1$.

4.2. The FENE- V model

The concept of an extra viscous stress in a dumbbell model was prompted by the failure of the elastic dumbbell models to quantitatively predict the stress in large De and highly transient

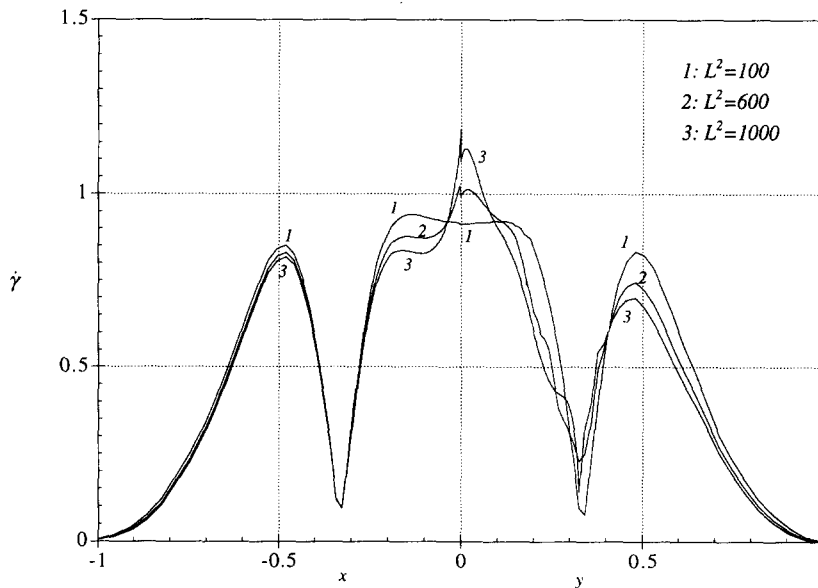


Fig. 19. Profiles of the strain rate $\dot{\gamma}$ along the axes for different values of L . $De = 1.34$, $c = 0.1$.

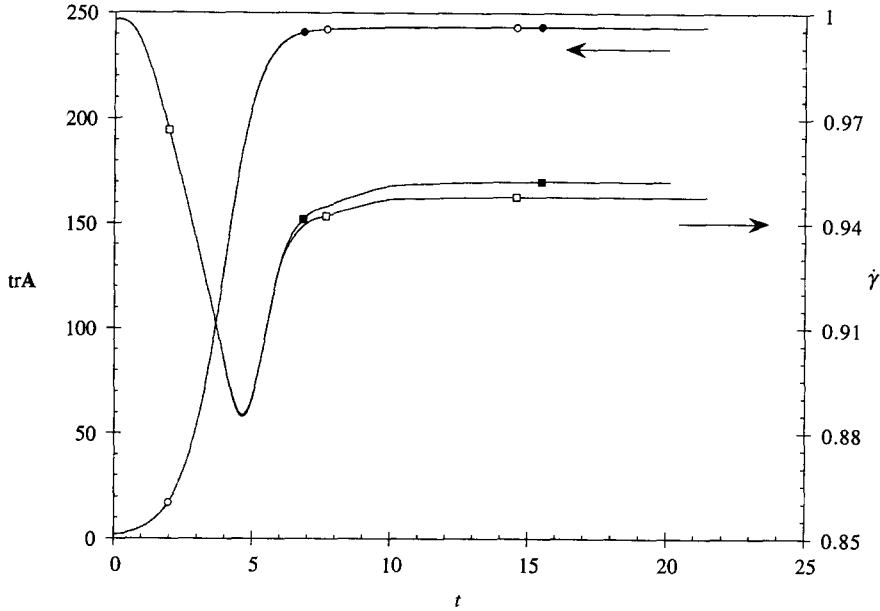


Fig. 20. Comparison of the evolution of $\dot{\gamma}$ and $\text{tr } \mathbf{A}$ at the stagnation point between the FENE-P and FENE-CR models. Filled symbols are for the FENE-P model and open ones for the CR model. $L^2 = 400$, $De = 1.34$, $c = 0.1$.

flows. For instance, unreasonably small values of L have to be used to fit rheological data; otherwise the measured stress is larger than can be accounted for by the elastic stress alone. The origin of the viscous stress is commonly believed to be the instantaneous rigidity of the polymer chain. Different pictures have been proposed for this instantaneous rigidity, including knots or self-entanglement [37], the ‘yo-yo’ configuration [38], ‘back-loops’ [39] and ‘kinks’ [40]. The latest effort along this line used computer simulations to directly study the conformation of a single model chain in an extensional flow [9,41]. A transient viscous stress is identified and modeled by an additional term in the FENE dumbbell model. Strictly speaking, this stress is not genuinely viscous as the polymer chains are not permanently rigid.

Another possible cause of viscous-like responses of polymer solutions is polydispersity. Even for polymer samples with narrow molecular weight distributions, there is a significant separation of the longest and shortest relaxation times. Modes faster than the response of the detector will be recorded as a viscous stress. In principle, this effect can be modeled by multimodal FENE models. It will be interesting to compare simulations of non-trivial flows based on the two different ideas. Experimentally, it appears impossible to distinguish between viscous stresses due to chain rigidity and faster elastic modes. Orr and Sridhar [42] have used the abrupt cessation of filament stretching to measure the relaxation of stresses. The resolution of short time scales proved to be a delicate matter and the identification of viscous stress is not without ambiguity.

We have done some preliminary simulations using the FENE-V model proposed by Rallison [9]. The deformation of the dumbbell is still described by Eq. (3). The polymer stress is changed from Eq. (2) to

$$\boldsymbol{\tau} = \frac{c\mu_s}{\lambda} \mathbf{A} + \alpha c\mu_s \frac{\mathbf{A}:\mathbf{D}}{\text{tr } \mathbf{A}} \mathbf{A}, \quad (7)$$

where $\mathbf{D} = [\nabla\mathbf{u} + (\nabla\mathbf{u})^T]/2$; α is a dimensionless parameter. Simulations in [9] suggest $\alpha = 0.5$. The second term is proportional to the strain rate and is thus viscous. The elastic stress contains only a linear spring force. As noted by Hinch [41], the viscous term will guarantee a plateau for the extensional viscosity at high strain rate, thus eliminating the need for a nonlinear spring. Further, using a linear spring force in the elastic stress gives the model a desirable feature as explained below. The nonlinear spring force is retained in describing the polymer’s deformation (Eq. (6)) to avoid unbounded extension of the dumbbell.

The FENE-V model can be compared with recent experimental measurements of Orr and Sridhar [42]. In an extensional flow of strain rate $\dot{\gamma}$, the viscous stress in Eq. (7) can be approximated by $\tau_v \approx \alpha c \mu_s \dot{\gamma} \mathbf{A}$ provided that the Deborah number $De = \lambda \dot{\gamma}$ exceeds the critical value for the coil-stretch transition. Thus the ratio of the magnitudes of the viscous and elastic stresses in Eq. (7) is

$$\frac{\tau_v}{\tau_e} = \alpha \lambda \dot{\gamma} = \alpha De. \tag{8}$$

This equation holds for uniaxial and planar extensional flows. If the nonlinear spring coefficient f is included in the elastic stress, the stress ratio will simply be a constant $\alpha/2$. Thus, omitting f is in fact necessary if the ratio τ_v/τ_e is to increase with the Deborah number, a feature that is evident in both simulations [9] and experiments [42]. By recording the relaxation from a transient uniaxial straining flow, Orr and Sridhar [42] determined a viscous stress that can be described by the following correlation:

$$\tau_v = \kappa \dot{\gamma} (\tau_e)^{1.65}, \tag{9}$$

where κ is a constant. It is easy to show, by using a FENE model for τ_e , that Eq. (9) differs from Eq. (8). A more quantitative comparison can be made based on a subset of data in [42] for which the strain rate $\dot{\gamma}$ is given. This data set fits Eq. (8) well with $\alpha = 0.872$. Therefore, the viscous stress estimated from Rallison’s simulations is smaller than that obtained experimentally over the De range studied ($1.66 \leq De \leq 3.17$), but the two are of the same order of magnitude.

Our calculations are done in dimensionless variables. The viscous term, if computed explicitly using the \mathbf{D} tensor of the previous time step, tends to cause numerical instability. We have solved the flow equation iteratively, updating the tensor \mathbf{D} in each iteration until convergence. Fig. 21 compares the evolution of $\dot{\gamma}$ and $\text{tr } \mathbf{A}$ at the stagnation point for the FENE-V model with the results for the FENE-CR model. There is a small initial overshoot in $\dot{\gamma}$ for the FENE-V model, and the steady-state strain rate is smaller than that for the CR model. The stretching of the polymer does not show any effect of the viscous stress at the beginning, but the steady-state value of $\text{tr } \mathbf{A}$ is also smaller than its FENE-CR counterpart. Away from the stagnation point, the viscous term causes a mild reduction in flow and polymer stretching. The velocity profile across the outgoing streamlines is shown in Fig. 22. Therefore, for this set of parameters, the main effect of the viscous stress is a mild reduction in flow and polymer stretching throughout the flow field. We have also tested $L^2 = 100$ and 400. The results are qualitatively the same though the magnitude of reductions in $\text{tr } \mathbf{A}$ and $\dot{\gamma}$ is smaller for smaller L .

In Fig. 19 we have noted that for large L values, the FENE-CR model predicts a curious increase in flow strength at the stagnation point. Experiments in the two-roll mill show that $\dot{\gamma}$ at the stagnation point attains the Newtonian values $\dot{\gamma}_0$ shortly after startup, and then decreases

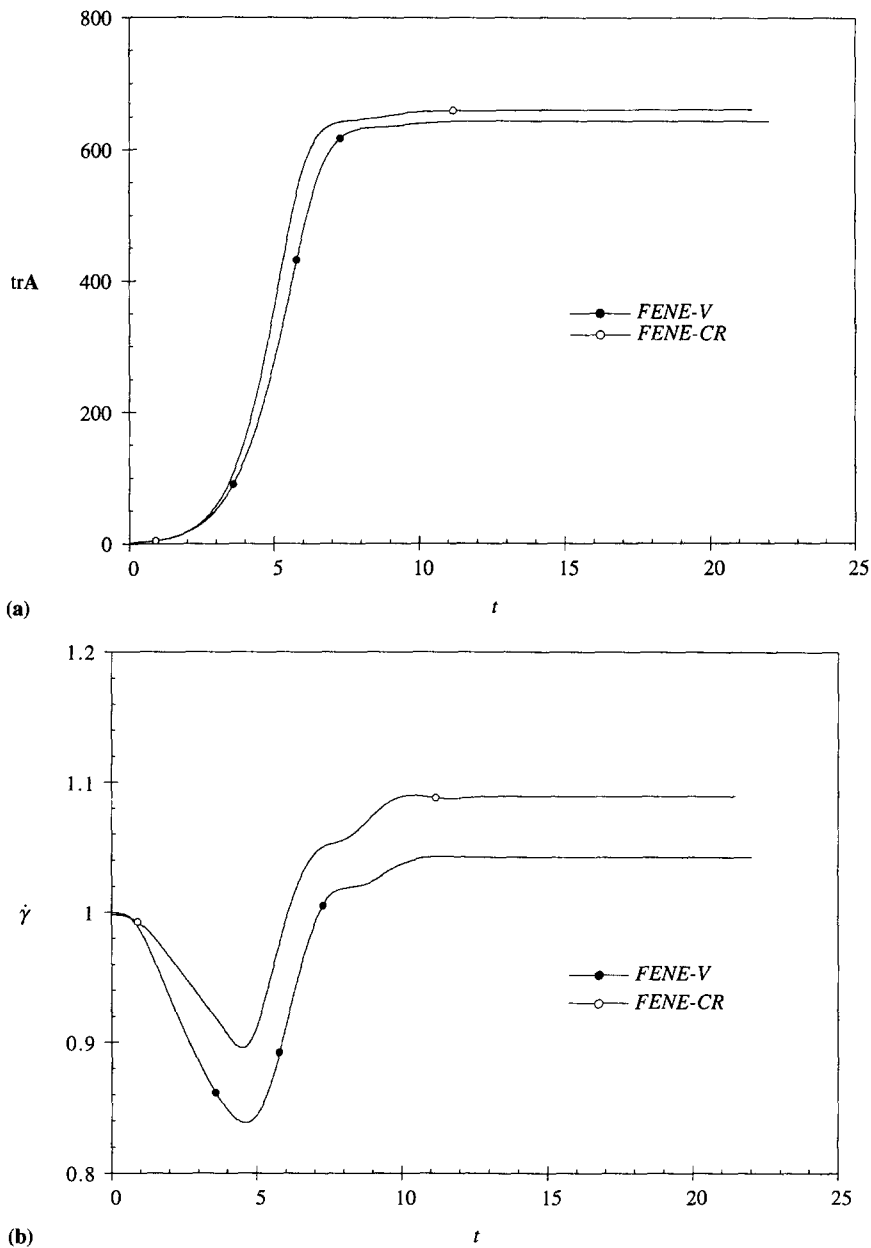


Fig. 21. Comparison of the evolution of (a) $\text{tr}\mathbf{A}$ and (b) $\dot{\gamma}$ at the stagnation point between the FENE-V and FENE-CR models. $L^2 = 1000$, $\text{De} = 1.34$, $c = 0.1$; $\alpha = 0.5$ for the FENE-V model.

toward a steady-state value which is smaller than $\dot{\gamma}_0$ [7]. The FENE-CR model, with the parameters fitted to the polystyrene solution used in the experiments ($c = 0.1$, $L^2 = 2500$), predicts a strain-rate greater than $\dot{\gamma}_0$ at the stagnation point. The predicted birefringence is about twice the measured value. This discrepancy seems to point to a defect of the FENE-CR model.

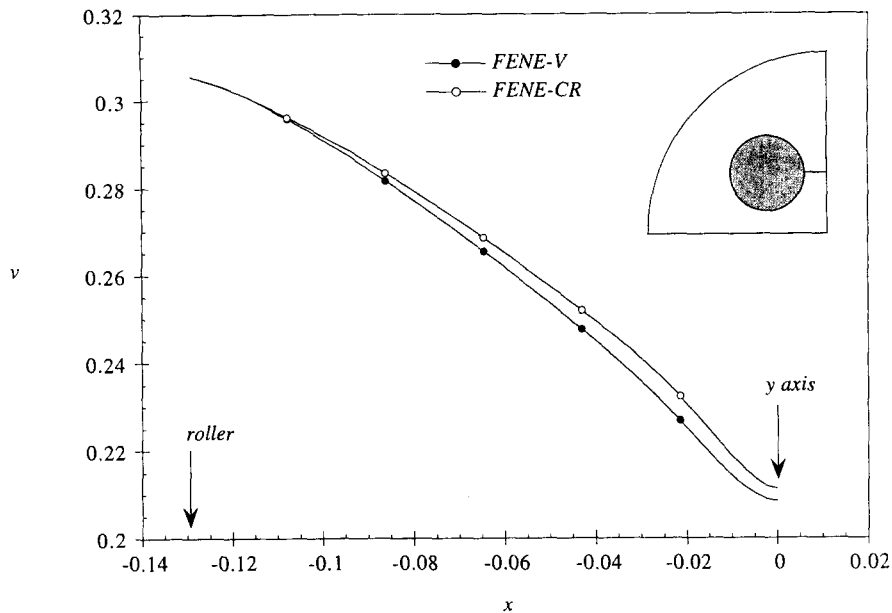


Fig. 22. Comparison of the velocity profile across the outflow streamlines at $y = 0.33$. The position of the profile is indicated by a horizontal line. $L^2 = 1000$, $De = 1.34$, $c = 0.1$; $\alpha = 0.5$ for the FENE-V model.

In this context, it is interesting that adding the viscous stress term reduces both $\dot{\gamma}$ and $\text{tr } \mathbf{A}$ at the stagnation point. For the parameters used here, the reduction in $\text{tr } \mathbf{A}$ is small and the steady-state $\dot{\gamma}$ is still above the Newtonian value. However, Fig. 21 demonstrates the possibility that a viscous stress effect may partly account for the discrepancy between theory and experiments.

To pursue this idea further one needs to undertake two tasks. First, the functional form and magnitude of the viscous stress must be firmly established. Currently there is much disagreement among the few results in the literature (see Eqs. (8) and (9)). Second, more comprehensive simulations should be carried out for a wide range of model parameters. In particular, parameter values appropriate for the polymer solutions used in experiments should be covered.

Besides viscous stress, other remedies have been proposed for the FENE-CR model in order to produce quantitative agreement with experiments. An interesting idea is the interaction among extended polymer chains that reduces chain extensions as well as flow modification [21]. A theory of interacting dumbbells has recently appeared [43].

5. Conclusions

The following conclusions can be drawn within the parameter ranges covered in this study. (i) Coupling between the flow field and the polymer configuration is such that the flow is suppressed and the polymer stretching is reduced. The region of significant flow suppression is much wider than the birefringent strand, within which the polymer is highly stretched. (ii) The

non-homogeneity of the flow has a profound effect on the flow-polymer coupling. Experiments done in non-homogeneous flows need be interpreted with caution; possible effects of non-homogeneous kinematics should be distinguished from the physical effects inherent in the flow-polymer coupling. (iii) The FENE-P model is not a good choice for studying the effects of shear-thinning because the amount of shear-thinning is not controllable and significant shear-thinning sets in only at very high Deborah numbers. This may not be a major shortcoming of the model, however, since the dilute solutions it proposes to model usually are not strongly shear-thinning. (iv) The extra viscous stress of Rallison [9] reduces the strain rate and polymer stretching at the stagnation point. Previous comparison with experiments in the two-roll mill has shown that the FENE-CR model over-predicts the birefringence and the strain rate. Thus, the viscous stress will probably bring model predictions closer to experiments. It is possible but not certain at present that the discrepancy between model predictions and experiments is in part due to the lack of a viscous stress contribution in the FENE-CR model.

Acknowledgements

This research was supported under grants from the Fluid Dynamics and Polymers programs at the National Science Foundation. The computation was done at the NSF Supercomputer Centers at San Diego and Pittsburgh. We thank Johan Remmelgas for his help with the code and many discussions.

References

- [1] B. Caswell, Report on the IXth International Workshop on Numerical Methods in Non-Newtonian Flows, *J. Non-Newtonian Fluid Mech.* 62 (1996) 99–110.
- [2] V. Tirtaatmadja, T. Sridhar, A filament stretching device for measurement of extensional viscosity, *J. Rheol.* 37 (1993) 1081–1102.
- [3] D.F. James, K. Walters, A critical appraisal of available methods for the measurements of extensional properties of mobile systems, in: A.A. Collyer (Ed.), *Techniques in Rheological Measurements*, Ch. 2, Chapman and Hall, 1993.
- [4] A.J. Szeri, S. Wiggins, L.G. Leal, On the dynamics of suspended microstructure in heterogeneous fluid flows, *J. Fluid Mech.* 228 (1991) 207–241.
- [5] L.G. Leal, Studies of flow-induced conformation changes in dilute polymer solutions, in: Y. Rabin (Ed.), *Polymer-Flow Interactions*, Proc. AIP Workshop, 137, 1985, pp. 5–32.
- [6] P. Singh, L.G. Leal, Computational studies of the FENE dumbbell model in a co-rotating two-roll mill, *J. Rheol.* 38 (1994) 485–517.
- [7] G.M. Harrison, J. Remmelgas, L.G. Leal, Dynamics of polymer solutions in transient flow: comparison of dumbbell-based theory and experiments (to appear).
- [8] P. Singh, L.G. Leal, Computational studies of the FENE bumbbell model with conformation dependent friction in a co-rotating two-roll mill, *J. Non-Newtonian Fluid Mech.* 67 (1996) 137–178.
- [9] J.M. Rallison, Dissipative stresses in dilute polymer solutions, *J. Non-Newtonian Fluid Mech.* 68 (1997) 61–83.
- [10] F.G. Frank, A. Keller, M.R. Mackley, Polymer chain extension produced by impinging jets and its effect on polyethylene solution, *Polymer* 12 (1971) 467–473.
- [11] F.G. Frank, M.R. Mackley, Localized flow birefringence of polyethylene oxide solutions in a two roll mill, *J. Polymer Sci., Polym. Phys. Ed.* 14 (1976) 1121–1131.

- [12] D.G. Crowley, F.C. Frank, M.R. Mackley, R.G. Stephenson, Localized flow birefringence of polyethylene oxide solutions in a four roll mill, *J. Polymer Sci., Polym. Phys. Ed.* 14 (1976) 1111–1119.
- [13] K. Gardner, E.R. Pike, M.J. Miles, A. Keller, K. Tanaka, Photon-correlation velocimetry of polystyrene solutions in extensional flow fields, *Polymer* 23 (1982) 1435–1442.
- [14] R. Cressely, R. Hocquart, O. Scrivener, Birefringence d'écoulement dans un dispositif à deux rouleaux, *Optica Acta* 25, (1978) 559–571.
- [15] R. Cressely, R. Hocquart, O. Scrivener, Lignes de biréfringence localisée dans un dispositif à deux rouleaux tournant en sens contraire, *Optica Acta* 26 (1979) 1173–1181.
- [16] A. Lyazid, O. Scrivener, R. Teitgen, Velocity field in an elongational polymer solution flow, in: G. Astarita et al. (Eds.), *Rheology*, vol. 2: Fluids, Plenum, 1980, pp. 141–148.
- [17] R. Cressely and R. Hocquart, Dynamics of flexible and large macromolecules in elongational flow. in: G. Astarita et al. (Eds.), *Rheology*, vol. 2: Fluids, Plenum, 1980, pp. 377–383.
- [18] G.G. Fuller, L.G. Leal, Flow birefringence of dilute polymer solutions in two-dimensional flows, *Rheol. Acta* 19 (1980) 580–600.
- [19] P.N. Dunlap, L.G. Leal, Dilute polystyrene solutions in extensional flow: birefringence and flow modification, *J. Non-Newtonian Fluid Mech.* 23 (1987) 5–48.
- [20] P.N. Dunlap, C.H. Wang, L.G. Leal, An experimental study of dilute polyelectrolyte solutions in strong flows, *J. Polym. Sci., Polym. Phys. Ed.* 25 (1987) 2211–2238.
- [21] R.C.-Y. Ng, L.G. Leal, Concentration effects on birefringence and flow modification of semidilute polymer solutions in extensional flow, *J. Rheol.* 37 (1993) 443–468.
- [22] G.G. Fuller, L.G. Leal, Flow birefringence of concentrated polymer solutions in two-dimensional flows, *J. Polym. Sci., Polym. Phys. Ed.* 19 (1981) 557–587.
- [23] E. Geffroy, L.G. Leal, Flow birefringence studies in transient flows of a two-roll mill for the test-fluid M1, *J. Non-Newtonian Fluid Mech.* 35 (1990) 361–400.
- [24] E. Geffroy, L.G. Leal, Flow birefringence studies of a concentrated polystyrene solution in a two-roll mill, I, steady flow and start-up of steady flow, *J. Polym. Sci., Polym. Phys. Ed.* 30 (1992) 1329–1349.
- [25] D. Yavich, D.W. Mead, L.G. Leal, Experimental studies of an entangled polystyrene solution in mixed type flows, Part 1, steady state; Part 2, transient flows (submitted to *J. Rheol.*).
- [26] A. Keller, J.A. Odell, The extensibility of macromolecules in solution: a new focus for macromolecular science, *Colloid Polym. Sci.* 263 (1985) 181–201.
- [27] A. Keller, A.J. Müller, J.A. Odell, Entanglement in semi-dilute solutions as revealed by elongational flow studies, *Prog. Colloid Polym. Sci.* 75 (1987) 179–200.
- [28] R.B. Bird, C.C. Curtiss, R.C. Armstrong, O. Hassager, *Dynamics of Polymeric Liquids*, vol. 2, Kinetic Theory, 2nd ed., Wiley, 1987.
- [29] M.D. Chilcott, J.M. Rallison, Creeping flow of dilute polymer solutions past cylinders and spheres, *J. Non-Newtonian Fluid Mech.* 29 (1988) 381–432.
- [30] P. Singh, L.G. Leal, Finite-element simulation of the start-up problem for a viscoelastic fluid in an eccentric rotating cylinder geometry using a third-order upwind scheme, *Theor. Comput. Fluid Dyn.* 5 (1993) 107–137.
- [31] G.G. Fuller, L.G. Leal, The effects of conformation-dependent friction and internal viscosity on the dynamics of the nonlinear dumbbell model for a dilute polymer solution, *J. Non-Newtonian Fluid Mech.* 8 (1981) 271–310.
- [32] O.G. Harlen, E.J. Hinch, J.M. Rallison, Birefringent pipe: the steady flow of a dilute polymer solution near a stagnation point, *J. Non-Newtonian Fluid Mech.* 44 (1992) 229–265.
- [33] O.J. Harris, J.M. Rallison, Start-up of a strongly extensional flow of a dilute polymer solution, *J. Non-Newtonian Fluid Mech.* 50 (1993) 89–124.
- [34] J.J. Wang, D. Yavich, L.G. Leal, Time-resolved velocity gradient and optical anisotropy in linear flow by photon correlation spectroscopy, *Phys. Fluids* 6 (1994) 3519–3534.
- [35] R.B. Bird, P.J. Dotson, N.L. Johnson, Polymer solution rheology based on a finitely extensible bead-spring chain model, *J. Non-Newtonian Fluid Mech.* 7 (1980) 213–235.
- [36] Y. Mochimaru, Fast squeezing flow of viscoelastic fluids, *J. Non-Newtonian Fluid Mech.* 9 (1981) 157–178.
- [37] D.H. King, D.F. James, Analysis of the Rouse model in extensional flow, Part II, Stress generated in sink flow by flexible macromolecules and by finitely extended macromolecules, *J. Chem. Phys.* 78 (1983) 4749–4754.

- [38] G. Ryskin, Calculation of the effect of polymer additive in a converging flow, *J. Fluid Mech.* 178 (1987) 423–440.
- [39] J.M. Rallison, E.J. Hinch, Do we understand the physics in the constitutive equation?, *J. Non-Newtonian Fluid Mech.* 29 (1988) 37–55.
- [40] R.G. Larson, The unraveling of a polymer chain in a strong extensional flow, *Rheol. Acta* 29 (1990) 371–384.
- [41] E.J. Hinch, Uncoiling of a polymer molecule in a strong extensional flow, *J. Non-Newtonian Fluid Mech.* 54 (1994) 209–230.
- [42] N.V. Orr, T. Sridhar, Stress relaxation in uniaxial extension, *J. Non-Newtonian Fluid Mech.* 67 (1996) 77–103.
- [43] C. Schneggenburger, M. Kroger, S. Hess, An extended FENE dumbbell theory for concentration dependent shear-induced anisotropy in dilute polymer solutions, *J. Non-Newtonian Fluid Mech.* 62 (1996) 235–251.